NASA/TM—2013-216619

Empirical Study of the Multiaxial, Thermomechanical Behavior of NiTiHf Shape Memory Alloys

Dhwanil Shukla
California Institute of Technology, Pasadena, California

Ronald D. Noebe
Glenn Research Center, Cleveland, Ohio

Aaron P. Stebner
California Institute of Technology, Pasadena, California

December 2013

NASA STI Program . . . in Profile

Since its founding, NASA has been dedicated to the advancement of aeronautics and space science. The NASA Scientific and Technical Information (STI) program plays a key part in helping NASA maintain this important role.

The NASA STI Program operates under the auspices of the Agency Chief Information Officer. It collects, organizes, provides for archiving, and disseminates NASA's STI. The NASA STI program provides access to the NASA Aeronautics and Space Database and its public interface, the NASA Technical Reports Server, thus providing one of the largest collections of aeronautical and space science STI in the world. Results are published in both non-NASA channels and by NASA in the NASA STI Report Series, which includes the following report types:

- TECHNICAL PUBLICATION. Reports of completed research or a major significant phase of research that present the results of NASA programs and include extensive data or theoretical analysis. Includes compilations of significant scientific and technical data and information deemed to be of continuing reference value. NASA counterpart of peer-reviewed formal professional papers but has less stringent limitations on manuscript length and extent of graphic presentations.

- TECHNICAL MEMORANDUM. Scientific and technical findings that are preliminary or of specialized interest, e.g., quick release reports, working papers, and bibliographies that contain minimal annotation. Does not contain extensive analysis.

- CONTRACTOR REPORT. Scientific and technical findings by NASA-sponsored contractors and grantees.

- CONFERENCE PUBLICATION. Collected papers from scientific and technical conferences, symposia, seminars, or other meetings sponsored or cosponsored by NASA.

- SPECIAL PUBLICATION. Scientific, technical, or historical information from NASA programs, projects, and missions, often concerned with subjects having substantial public interest.

- TECHNICAL TRANSLATION. English-language translations of foreign scientific and technical material pertinent to NASA's mission.

Specialized services also include creating custom thesauri, building customized databases, organizing and publishing research results.

For more information about the NASA STI program, see the following:

- Access the NASA STI program home page at *http://www.sti.nasa.gov*

- E-mail your question to *help@sti.nasa.gov*

- Fax your question to the NASA STI Information Desk at 443–757–5803

- Phone the NASA STI Information Desk at 443–757–5802

- Write to:
  STI Information Desk
  NASA Center for AeroSpace Information
  7115 Standard Drive
  Hanover, MD 21076–1320

NASA/TM—2013-216619

Empirical Study of the Multiaxial, Thermomechanical Behavior of NiTiHf Shape Memory Alloys

Dhwanil Shukla
California Institute of Technology, Pasadena, California

Ronald D. Noebe
Glenn Research Center, Cleveland, Ohio

Aaron P. Stebner
California Institute of Technology, Pasadena, California

National Aeronautics and
Space Administration

Glenn Research Center
Cleveland, Ohio 44135

December 2013

Acknowledgments

This work was supported by the NASA FAP Aeronautical Sciences Project, Technical Discipline Lead Dale Hopkins. Dhwanil Shukla is grateful to the SURF program at the California Institute of Technology for supporting the summer internship that made this work possible.

This report contains preliminary findings, subject to revision as analysis proceeds.

Level of Review: This material has been technically reviewed by technical management.

Available from

NASA Center for Aerospace Information
7115 Standard Drive
Hanover, MD 21076–1320

National Technical Information Service
5301 Shawnee Road
Alexandria, VA 22312

Available electronically at http://www.sti.nasa.gov

Empirical Study of the Multiaxial, Thermomechanical Behavior of NiTiHf Shape Memory Alloys

Dhwanil Shukla
California Institute of Technology
Pasadena, California 91125

Ronald D. Noebe
National Aeronautics and Space Administration
Glenn Research Center
Cleveland, Ohio 44135

Aaron P. Stebner
California Institute of Technology
Pasadena, California 91125

Abstract

An empirical study was conducted to characterize the multiaxial, thermomechanical responses of new high temperature NiTiHf alloys. The experimentation included loading thin walled tube $Ni_{50.3}Ti_{29.7}Hf_{20}$ alloy samples along both proportional and nonproportional axial-torsion paths at different temperatures while measuring surface strains using stereo digital image correlation. A $Ni_{50.3}Ti_{33.7}Hf_{16}$ alloy was also studied in tension and compression to document the effect of slightly depleting the Hf content on the constitutive responses of NiTiHf alloys. Samples of both alloys were made from nearly texture free polycrystalline material processed by hot extrusion. Analysis of the data shows that very small changes in composition significantly alter NiTiHf alloy properties, as the austenite finish (A_f) temperature of the 16-at.% Hf alloy was found to be ~60 °C less than the 20-at.% Hf alloy (~120 vs. 180 °C). In addition, the 16-at.% Hf alloy exhibited smaller compressive transformation strains (2 vs. 2.5 percent). Multi-axial characterization of the 20-at.% Hf alloy showed that while the random polycrystal transformation strains in tension (4 percent) and compression (2.5 percent) are modest in comparison with binary NiTi (6 percent, 4 percent), the torsion performance is superior (7 vs. 4 percent shear strain width to the pseudoelastic plateau).

1.0 Introduction

Shape Memory Alloys (SMAs) are novel materials that have the ability to return from a deformed state to a previously "memorized" shape. This ability results in two fundamental shape memory behaviors: (1) shape memory effect (SME) and (2) pseudoelasticity. Both behaviors occur because of the diffusionless, solid-state phase transformation between a high symmetry austenite phase and a low symmetry martensite phase. SME is exhibited when the phase transformation is induced by a change in temperature (martensite phase transforms to austenite on heating at a temperature beyond the austenite finish (A_f) temperature) (Ref. 1). If a mechanical load is applied while the temperature is cycled, work may be performed during the transformation through the SME, as an SMA is able to recover the deformation imposed upon the martensite even in the presence of an applied load. Psuedoelasticity results from the stress-induced transformation of austenite to martensite at temperatures above the austenite finish temperature (Ref. 2). An SMA can be engineered to exhibit pseudoelasticity or SME at a targeted temperature by controlling the transformation temperatures through alloying and aging (Refs. 1 to 3).

Of the various material systems capable of shape memory behaviors, polycrystalline NiTi is the most widely used in commercial applications and is central to a number of biomedical and industrial applications (Refs. 1 and 3). However, a major limitation of binary NiTi alloys is relatively low transformation temperatures (<100 °C), which restricts the potential applications for these types of materials. Hf may be substituted for Ti in shape memory alloy compositions of NiTi to achieve properties that are not exhibited by binary NiTi alloys (Ref. 4), in particular, an elevation of the transformation temperatures. For the specific alloys studied in this work, the Hf substitution resulted in a moderate increase in transformation temperatures such that the austenite start temperatures were greater than 100 °C.

Previous studies characterizing the thermomechanical behavior of related NiTiHf alloys were limited, both in the range of compositions studied and in examination of only uniaxial loading (Refs. 5 to 9). Highly non-linear and anisotropic responses of NiTiHf are expected, even in randomly textured polycrystals, due to the phase transformation between a non-centrosymmetric martensite phase and a centrosymmetric austenite phase (Refs. 1 and 2). Thus, it is difficult to infer three-dimensional behavior of NiTiHf shape memory alloys from uniaxial tests.

Thus, this study was aimed at characterizing the multi-axial (tension, torsion, compression, and combined tension-torsion and compression-torsion) response of a $Ni_{50.3}Ti_{29.7}Hf_{20}$ alloy. Based on earlier studies (Refs. 5, 7 to 9), it is known that this alloy exhibits good uniaxial actuation and psuedoelastic properties. In addition, we investigated a slightly different $Ni_{50.3}Ti_{33.7}Hf_{16}$ alloy in tension and compression to document the change in properties of this alloy system in response to small changes in Hf content, building on previous efforts on a $Ni_{50.3}Ti_{34.7}Hf_{15}$ alloy (Ref. 6), which only went as far as characterizing basic transformation behaviors but not mechanical or functional properties.

2.0 Experimental Procedures

2.1 Material Description and Corresponding Sample Geometries

The NiTiHf alloys used in this investigation were parts of two larger heats of Ni-rich NiTiHf (at.%) produced by Flowserve Corporation, Dayton, Ohio, by a cold-crucible vacuum induction melting process. In both cases, the cast ingots were vacuum homogenized at 1050 °C for 72 h, followed by extrusion at 900 °C. Details of the two alloys and subsequent test samples are as follows.

2.1.1 $Ni_{50.3}Ti_{29.7}Hf_{20}$ Alloy Samples From Flowserve Heat no. 1:

Material Composition (at.%)

1. Nickel: 50.3 percent
2. Hafnium: 20 percent
3. Titanium: 29.7 percent

Heat Treatment

As-extruded material subsequently aged at 550 °C for 3 hr.

Sample Geometry

Samples of this alloy were frabricated with thin walled tube gage sections, along with a hex and threaded stud on both ends for gripping purposes (Fig. 1). The tube geometry was chosen for multiaxial characterization of this alloy to allow for analysis to be carried out assuming the shear stress in the gage was uniform.

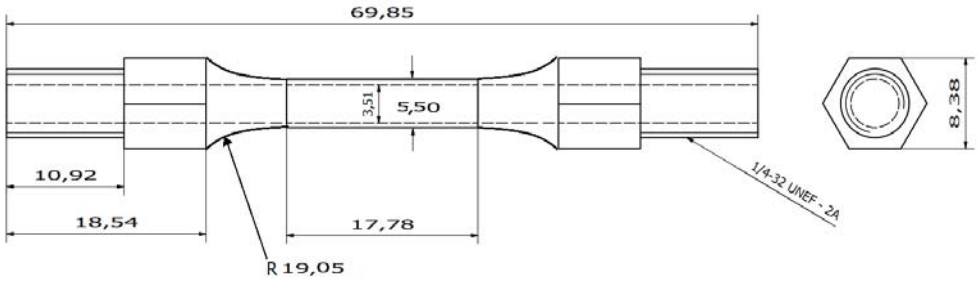

Figure 1.—$Ni_{50.3}Ti_{29.7}Hf_{20}$ alloy multiaxial sample geometry. (Dimensions are in mm.)

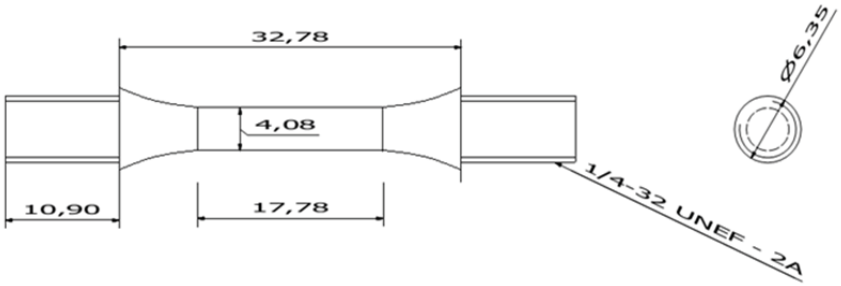

Figure 2.—$Ni_{50.3}Ti_{33.7}Hf_{16}$ alloy tension-compression sample geometry. (Dimensions are in mm.)

2.1.2 $Ni_{50.3}Ti_{33.7}Hf_{16}$ Alloy Samples From Flowserve Heat no. 2a

Material Composition (at.%)

1. Nickel: 50.3 percent
2. Hafnium: 16 percent
3. Titanium: 33.7 percent

Heat Treatment

As-extruded material subsequently aged at 550 °C for 3 hr.

Sample Geometry

The solid cylindrical dogbone tension-compression sample geometry consisted of a central gauge section with threaded studs on both ends for gripping purposes (Fig. 2).

2.2 Test Setup

2.2.1 Load Frame

A hydraulic MTS (Material Test System) 3.3 kip (15 kN) axial-axis, 1300 lbf-in. (150 N-m) torsion-axis load frame was used to apply axial and torsional stress to the samples. Custom high-temperature capable water-cooled Inconel grips were used for holding the sample. Figure 3 shows the MTS load frame with the Inconel grips installed.

2.2.2 Furnace and Temperature Control

A 10 kW induction furnace (Fig. 4**)** with remote work-head and a custom-wound copper induction coil was used to control the sample thermal loading during testing. Other instrumentation used in thermal control included the water circulation unit (Fig. 5) for pumping chilled water to the induction coil and Inconel grips and the temperature controller (Fig. 6). Type K thermocouples were used for measuring the sample surface temperature.

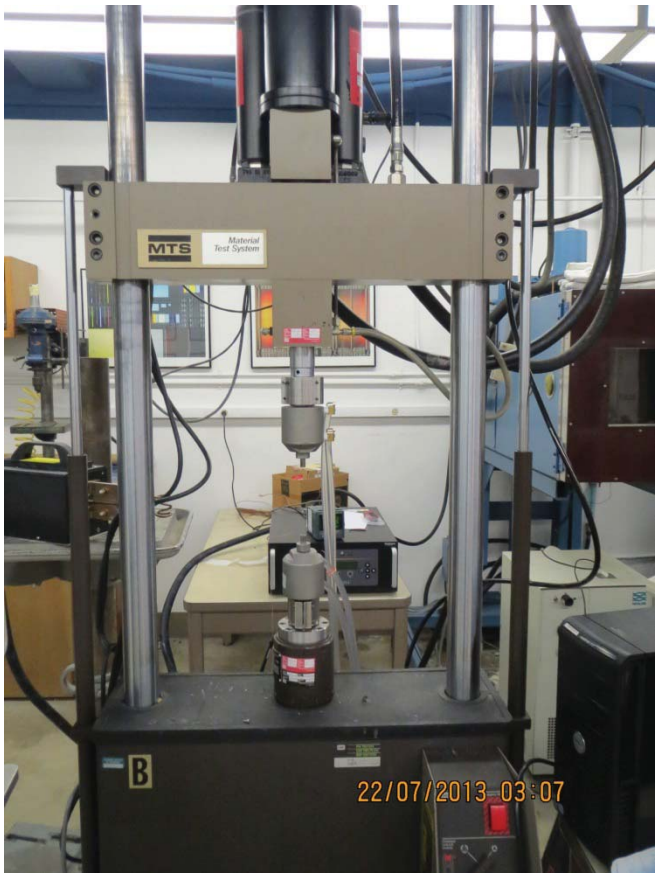

Figure 3.—MTS load frame with Inconel grips.

Figure 4.—Induction furnace and controller.

Figure 5.—Water circulation system.

Figure 6.—Temperature controller.

Figure 7.—Laser extensometer.

Figure 8.—Components of the DIC system.

2.2.3 Laser Extensometer

A laser extensometer (Fig. 7) was used for non-contact measurement of strains in the $Ni_{50.3}Ti_{33.7}Hf_{16}$ alloy samples during uniaxial testing.

2.2.4 Digital Image Correlation System (DIC)

The surface displacements of the $Ni_{50.3}Ti_{29.7}Hf_{20}$ alloy samples were measured using DIC. Images of a painted pattern on the surface of the samples were acquired from two cameras located slightly separated from each other in space (binocular for 3D information capture). These photographs were then processed by image processing software, which tracks the movement of each speckle through the series of images providing the displacement of each speckle. This displacement data is then used to determine surface strains. The components of our DIC system include the following (Fig. 8):

1. Two Cameras with lenses—for binocular images
2. Camera stand—for keeping cameras stable and in position
3. Lamp—for providing adequate high-intensity lighting for taking pictures
4. DAQ (National Instruments)—for relaying signals from other sensors and devices
5. PC with 3D correlation software—for performing image processing to determine displacements and strains

2.3 Loading Program Segment Types

The Type I to VII loading program segments described below were conducted only on the $Ni_{50.3}Ti_{29.7}Hf_{20}$ alloy samples while the Type A, B, and C loading program segments were conducted only on the $Ni_{50.3}Ti_{33.7}Hf_{16}$ alloy samples.

2.3.1 $Ni_{50.3}Ti_{29.7}Hf_{20}$ Alloy Samples

Unique proportional and non-proportional mechanical loading paths were imposed upon the tubular specimens. We have defined the types of loading paths used in the experiments as follows, with graphical depictions shown in Figure 9.

Type I: ***Proportional Tension***:

a. Load in tension to a predetermined force linearly in force control.
b. Unload tension back to zero force linearly in force control.

Type II: ***Proportional Compression***:

a. Load in compression to a predetermined force linearly in force control.
b. Unload compression back to zero force linearly in force control.

Type III: ***Proportional Torsion***:

a. Load in torsion to a predetermined rotation angle linearly in rotation control.
b. Unload torsion back to zero angle linearly in rotation control.

Type IV: ***Non-Proportional Axial-Torsion (ATTA)***:

a. Load in **A**xial direction to a particular displacement linearly in displacement control.
b. Load in **T**orsion to a particular rotation angle linearly in rotation control.
c. Unload **T**orsion back to zero angle linearly in rotation control.
d. Unload **A**xially back to zero displacement linearly in displacement control.

Type V: ***Non-Proportional Axial-Torsion (ATAT)***:

a. Load in **A**xial direction to a particular displacement linearly in displacement control.
b. Load in **T**orsion to a particular rotation angle linearly in rotation control.
c. Unload **A**xially back to zero displacement linearly in displacement control.
d. Unload **T**orsion back to zero angle linearly in rotation control.

Thus, the loading programs of Type IV and V have the same loading paths (a, b) but different unloading paths (c, d).

Type VI: ***Proportional Axial-Torsion (AT)(AT)***:

a. Load in **A**xial and **T**orsional direction simultaneously to a predetermined displacement and rotation in simultaneous displacement and rotation control.
b. Unload in **A**xial and **T**orsional direction to zero displacement and angle in simultaneous displacement and rotation control.

Type VII: ***Fixed Crosshead Thermal Cycling***:

a. Changing temperature while keeping crossheads locked (fixed in displacement and rotation).

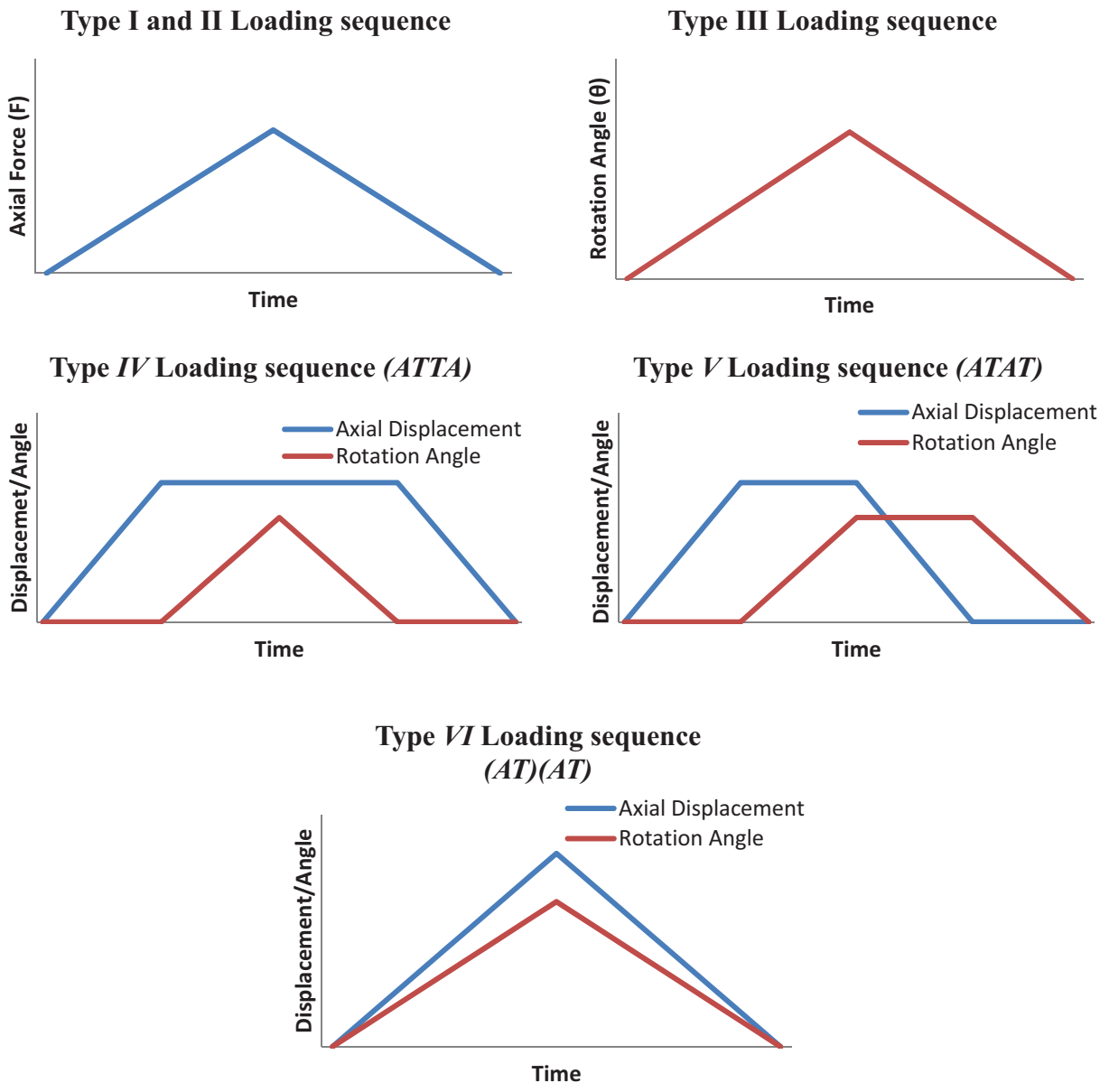

Figure 9.—Graphical representations of the loading programs used to test the $Ni_{50.3}Ti_{29.7}Hf_{20}$ alloy samples.

2.3.2 $Ni_{50.3}Ti_{29.7}Hf_{16}$ Alloy Samples

Type A*: *Constant Force Thermal Cycling:

a. Load in tension or compression to a particular force.
b. Heat sample to a specific temperature linearly at some specific rate keeping the applied force constant.
c. Cool sample by switching off furnace keeping force constant.

Type B*: *Constant Temperature Mechanical Cycling:

a. Heat and maintain sample at predetermined temperature.
b. Load in tension/compression to a particular force linearly keeping temperature constant.
c. Unload to zero force linearly with same rate keeping temperature constant.

Type C*: *Blocking Stress Test:

a. Load the sample to particular displacement value.
b. Heat sample to a particular temperature linearly with time keeping displacement constant.
c. Cool back to room temperature keeping displacement constant.

2.4 Complete Test Sequences for the $Ni_{50.3}Ti_{29.7}Hf_{20}$ Samples

Testing was conducted on four samples. Sample 1 was loaded in compression at 180 °C with fixed 0° rotation to a force of –9 kN and then unloaded. Sample 2 was loaded in tension at 180 °C with fixed 0° rotation until fracture occurred in the grips. Sample 3 was subjected to a sequence of tension—torsion steps defined in Section 2.4.1 and Sample 4 was subjected to a sequence of compression—torsion steps defined in Section 2.4.2. The complete loading histories of Samples 3 and 4 follow.

2.4.1 Sample 3—Tension-Torsion

1. 0 N axial force, 0° rotation control, temperature cycled between 250 °C and room temperature twice
2. 0 N axial force, 0° rotation control, temperature increased to 180 °C
3. *Type I* loading: load to 4950 N (~0.8 GPa) axial force, 0° rotation control, while temperature maintained at 180 °C
4. *Type III* loading: 0 N axial force, twist to 90° rotation angle, temperature maintained at 180 °C
5. *Type IV* loading: load to axial displacement corresponding to ~2 percent axial strain, twist to 90° rotation angle, temperature maintained at 180 °C
6. *Type V* loading: load to axial displacement corresponding to ~2 percent axial strain, twist to 90° rotation angle, temperature maintained at 180 °C
7. *Type VI* loading: load to axial displacement corresponding to ~2 percent axial strain, twist to 90° rotation angle, temperature maintained at 180 °C
8. *Type VII* loading: displacement fixed, rotation angle fixed, temperature cycled between 250 °C and room temperature twice
9. *Type VII* loading: displacement fixed, rotation angle fixed, heat to 220 °C
10. *Type I* loading: load to 4950 N (~0.8 GPa) axial force, 0° rotation control, while temperature maintained at 220 °C
11. *Type III* loading: 0 N axial force, twist to 90° rotation angle, temperature maintained at 220 °C
12. *Type VI* loading: load to axial displacement corresponding to ~2 percent axial strain, twist to 90° rotation angle, temperature maintained at 220 °C
13. *Type IV* loading: load to axial displacement corresponding to ~2 percent axial strain, twist to 90° rotation angle, temperature maintained at 220 °C
14. *Type V* loading: load to axial displacement corresponding to ~2 percent axial strain, twist to 90° rotation angle, temperature maintained at 220 °C

15. Unload axial and torsional stresses, while maintaining temperature at 220 °C
16. 0 N axial force, 0 N-m torque, decrease temperature to RT
17. Unload

2.4.2 Sample 4—Compression-Torsion

1. 0 N axial force, 0° rotation control, temperature cycled between 250 °C and room temperature twice
2. 0 N axial force, 0° rotation control, temperature increase to 180 °C
3. *Type II* loading: load to –4950 N (~–0.8 GPa) axial force, 0° rotation control, temperature maintained at 180 °C
4. *Type III* loading: 0 N axial force, twist to 90° rotation angle, temperature maintained at 180 °C
5. *Type IV* loading: load to axial displacement corresponding to ~–2 percent axial strain, twist to 90° rotation angle, temperature maintained at 180 °C
6. *Type V* loading: load to axial displacement corresponding to ~–2 percent axial strain, twist to 90° rotation angle, temperature maintained at 180 °C
7. *Type VI* loading: load to axial displacement corresponding to ~–2 percent axial strain, twist to 90° rotation angle, temperature maintained at 180 °C
8. *Type VII* loading: displacement fixed, rotation angle fixed, temperature cycled between 250 °C and room temperature twice
9. *Type VII* loading: displacement fixed, rotation angle fixed, heat to 220 °C
10. *Type II* loading: load to –4950 N (~–0.8 GPa) axial force, 0° rotation control, temperature maintained at 220 °C
11. *Type III* loading: 0 N axial force, twist to 90° rotation angle, temperature maintained at 220 °C
12. *Type VI* loading: load to axial displacement corresponding to ~–2 percent axial strain, twist to 90° rotation angle, temperature maintained at 220 °C
13. *Type V* loading: load to axial displacement corresponding to ~–2 percent axial strain, twist to 90° rotation angle, temperature maintained at 220 °C
14. *Type IV* loading: load to axial displacement corresponding to ~–2 percent axial strain, twist to 90° rotation angle, temperature maintained at 220 °C
15. Unload axial and torsional stresses, while maintaining temperature at 220 °C
16. 0 N axial force, 0 N-m torque, decrease temperature to RT
17. Unload

2.5 Complete Test Sequences for the $Ni_{50.3}Ti_{33.7}Hf_{16}$ Samples

A total of seven samples were used to characterize the tension-compression behavior of the 16-at.% Hf alloy. Their loading histories follow.

2.5.1 Sample 1

1. Type A loading: –159 N (–10 MPa), 0 to 240 °C, two thermal cycles
2. Type A loading: –1587 N (–100 MPa), 0 to 240 °C, two thermal cycles
3. Type A loading: –3175 N (–200 MPa), 0 to 240 °C, two thermal cycles
4. Type A loading: –6350 N (–400MPa), 0 to 240 °C, two thermal cycles
5. Type A loading: 1587 N (100 MPa), 0 to 240 °C, two thermal cycles
6. Type A loading: 3175 N (200 MPa), 0 to 240 °C, two thermal cycles
7. The sample failed in the threads while loading to 6350 N (400 MPa)

2.5.2 Sample 2

1. Type B loading: 160 °C, –16740 N
2. Type B loading: 160 °C, –3736 N
3. Type B loading: 160 °C, –5990 N
4. Type B loading: 160 °C, –12000 N
5. Type B loading: 160 °C, –13000 N
6. Type B loading: 150 °C, –13000 N
7. Type B loading: 150 °C, –13000 N
8. Type B loading: 25 °C, –12000 N
9. Type B loading: 25 °C, –13000 N
10. Type A loading: –7729 N (–600 MPa), 0 to 240 °C, two thermal cycles
11. Type A loading: –10305 N (–800 MPa), 0 to 240 °C, two thermal cycles
12. Type A loading: –12882 N (–1000 MPa), 0 to 240 °C, two thermal cycles

2.5.3 Sample 3

1. Type A loading: –1288 N (–100 MPa), 0 to 240 °C, two thermal cycles
2. Type A loading: –2576 N (–200 MPa), 0 to 240 °C, two thermal cycles
3. Type A loading: –5153 N (–400 MPa), 0 to 240 °C, two thermal cycles
4. Type A loading: –7729 N (–600 MPa), 0 to 240, °C, two thermal cycles
5. Type A loading: –10306 N (–800 MPa), 0 to 240 °C, two thermal cycles
6. Type A loading: –12882 N (–1000 MPa), 0 to 240 °C, two thermal cycles
7. Type A loading: 0 MPa, 0 to 240 °C, two thermal cycles
8. Type B loading: 25 °C, –7729 N
9. Type A loading: 0 MPa, 0 to 240 °C, one thermal cycle
10. Type B loading: 25 °C, –10306 N
11. Type A loading: 0 MPa, 0 to 240 °C, one thermal cycle
12. Type B loading: 25 °C, –12882 N
13. Type A loading: 0 MPa, 0 to 240 °C, one thermal cycle

2.5.4 Sample 4

1. Type B loading: 25 °C, 7729 N
2. Type A loading: 0 MPa, 0 to 240 °C, one thermal cycle
3. Type B loading: 25 °C, 10306 N
4. Type A loading: 0 MPa, 0 to 240 °C, one thermal cycle
5. Type B loading: 25 °C, 10306 N
6. Type A loading: 0 N, 0 to 240 °C, one thermal cycle
7. Type B loading: 25 °C, –12882 N
8. Type A loading: 0 N, 0 to 240 °C one thermal cycle

2.5.5 Sample 5

1. Type A loading: 0 N, 0 to 240 °C, two thermal cycles
2. Type B loading: 25 °C, 7729 N
3. Type A loading: 0 N, 0 to 240 °C, one thermal cycle
4. Type B loading: 25 °C, 10306 N
5. Type A loading: 0 N, 0 to 240 °C, one thermal cycle
6. Type B loading: 25 °C, 10306 N
7. Type A loading: 0 N, 0 to 240 °C, one thermal cycle

8. Type B loading: 25 °C, –12882 N
9. Type A loading: 0 N, 0 to 240 °C, one thermal cycle

2.5.6 Sample 6

1. Type A loading: 0 N, 0 to 240 °C, two thermal cycles
2. Type C loading: displacement corresponding to ~–1 percent strain, 0 to 240 °C, two thermal cycles
3. Type C loading: displacement corresponding to ~–2.5 percent strain, 0 to 240 °C, two thermal cycles

2.5.7 Sample 7

1. Type A loading: 0 N, 0 to 240 °C, two thermal cycles
2. Type C loading: displacement corresponding to ~–0.5 percent strain, 0 to 240 °C, two thermal cycles
3. Unload sample in stress
4. Type A loading: 0 N, 0 to 240 °C, two thermal cycles
5. Type B loading: 25 °C, 5153 N
6. Type A loading: 0 N, 0 to 240 °C, two thermal cycles
7. Sample failed in threads at 558 MPa (1788 N) while trying to do Type B loading at 25 °C to 600 MPa (7729 N)

Note that throughout the test sequences above the step ‘Type A loading: 0 N, 0 to 240 °C two thermal cycles’ has been used for resetting the material into a stress-free state.

3.0 Results

The results of the experiments conducted in this study are primarily presented as plots of engineering equivalent stress and engineering equivalent strains. However, some plots are just engineering stress versus engineering strain plots. The equivalent stresses and strains are obtained by the expressions:

$$\sigma_{eq} = \sqrt{\sigma_a^2 + 3\sigma_t^2} \quad \text{and} \quad \varepsilon_{eq} = \sqrt{\left(\varepsilon_a^2 + \frac{4}{3}\varepsilon_t^2\right)} \tag{1}$$

respectively, where

σ_{eq} = Equivalent Engineering Stress
σ_a = Axial Engineering Stress
σ_t = Torsional Engineering Stress
ε_{eq} = Equivalent Engineering Strain
ε_a = Axial Engineering Strain
ε_t = Torsional Engineering Strain

3.1 $Ni_{50.3}Ti_{29.7}Hf_{20}$ Alloy Experimental Data

Note that the Type I to VII loading programs were conducted on the $Ni_{50.3}Ti_{29.7}Hf_{20}$ alloy samples only, while Type A, B, and C loading programs were conducted only on the $Ni_{50.3}Ti_{33.7}Hf_{16}$ alloy samples. The experimental results for the $Ni_{50.3}Ti_{29.7}Hf_{20}$ alloy samples are presented below in the same order as described in Section 2.4. Subsequent to inserting the samples into the grips, but prior to all deformations reported in this work, specimens were heated and cooled twice between room temperature and 240 °C in 0 load, 0 torque control. Nothing other than normal thermal expansion was observed, so these data are not reported. For each of the four samples, the complete data set for *each* load segment are reported in 6 subplots: (a) stress-strain, where axial, torsion, and Mises mechanical responses are shown; (b) effective axial versus torsion strain; (c) effective axial versus torsion stress; (d) axial force and displacement versus time; (e) torque and rotation versus time; and (f) standard deviation of the axial and shear strain calculations from the DIC analysis versus time.

3.1.1 Sample 1

The motivation for this test was to begin to test the limit of compression loading on the tube geometry. As the results in Figure 10 demonstrate, the sample geometry could be loaded successfully to 1.5 GPa in compression without any buckling.

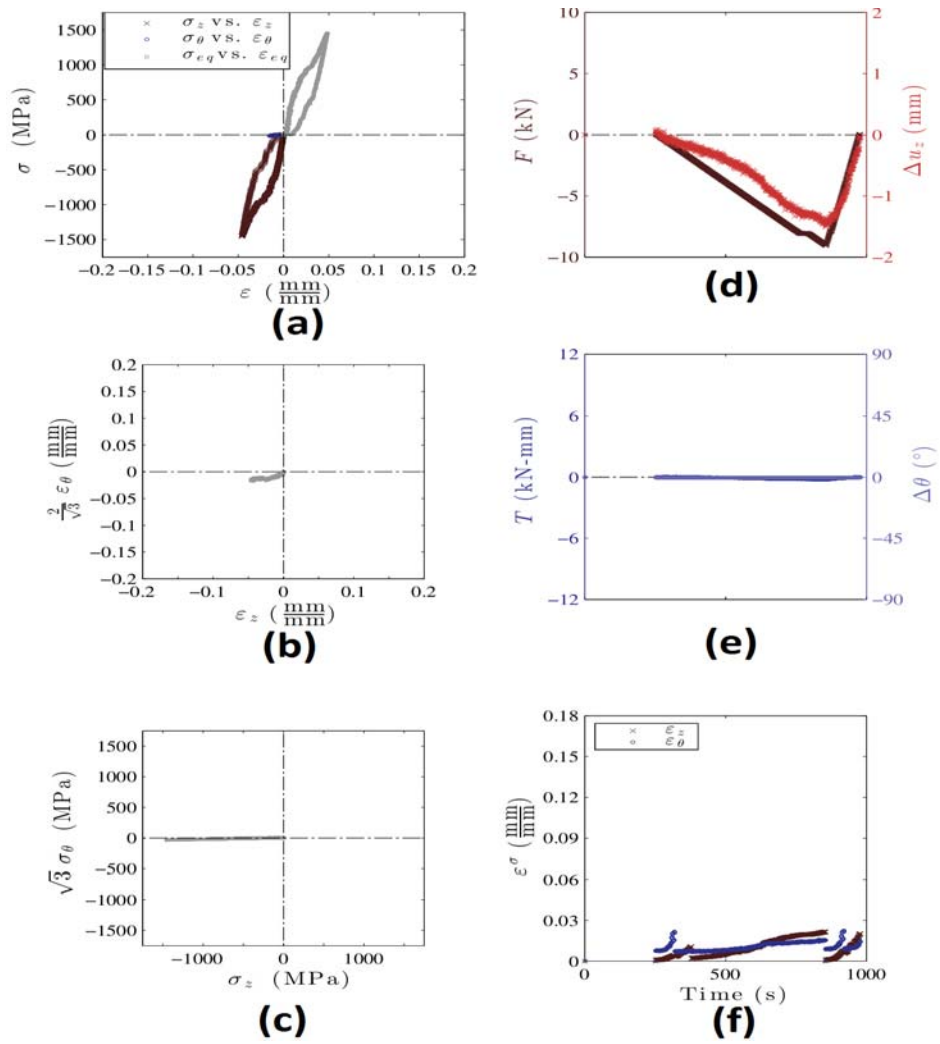

Figure 10.—$Ni_{50.3}Ti_{29.7}Hf_{20}$ Sample 1 responses.

3.1.2 Sample 2

The data in Figure 11 was obtained while attempting to run to 1.5 GPa in tension. The sample broke in the grip at the threads at about 1 GPa. Therefore, subsequent tests were restricted to loading to 0.8 GPa in tension to prevent failure of additional samples.

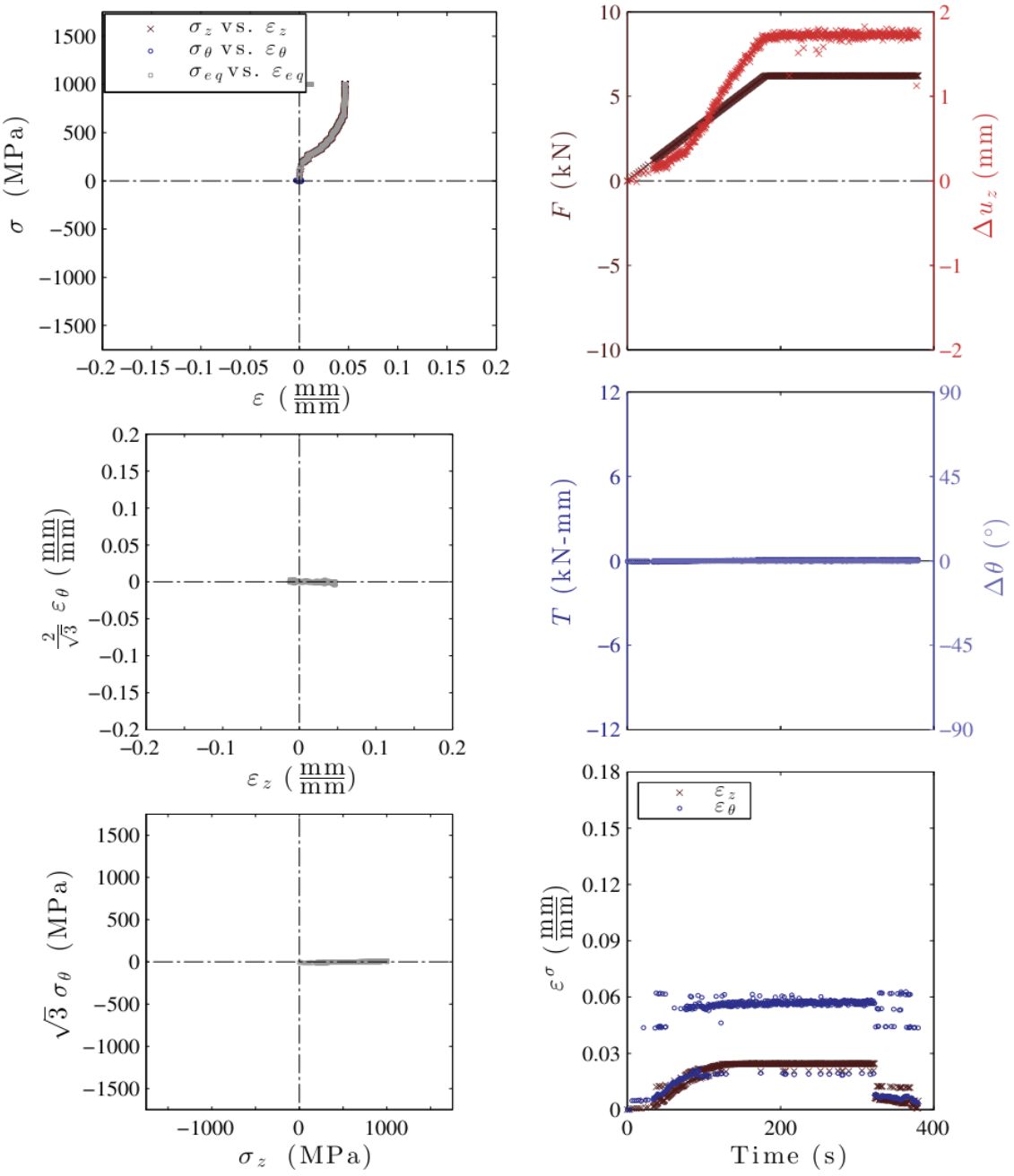

Figure 11.—$Ni_{50.3}Ti_{29.7}Hf_{20}$ Sample 2 responses.

3.1.3 Sample 3

This sample was utilized in performing a series of Tension-Torsion loading experiments at 180 and 220 °C. Refer to Section 2.4.1 for a complete loading history for the sample and for additional details of the various test sequence segments.

3.1.3.1 Type I Loading at 180 °C

Some slipping of the threads in the grips was observed during this test and resulted in the "steps" observed in the stress-strain curve. Adjustments were made to subsequent samples and the mechanical contact seemed to stabilize in subsequent tests.

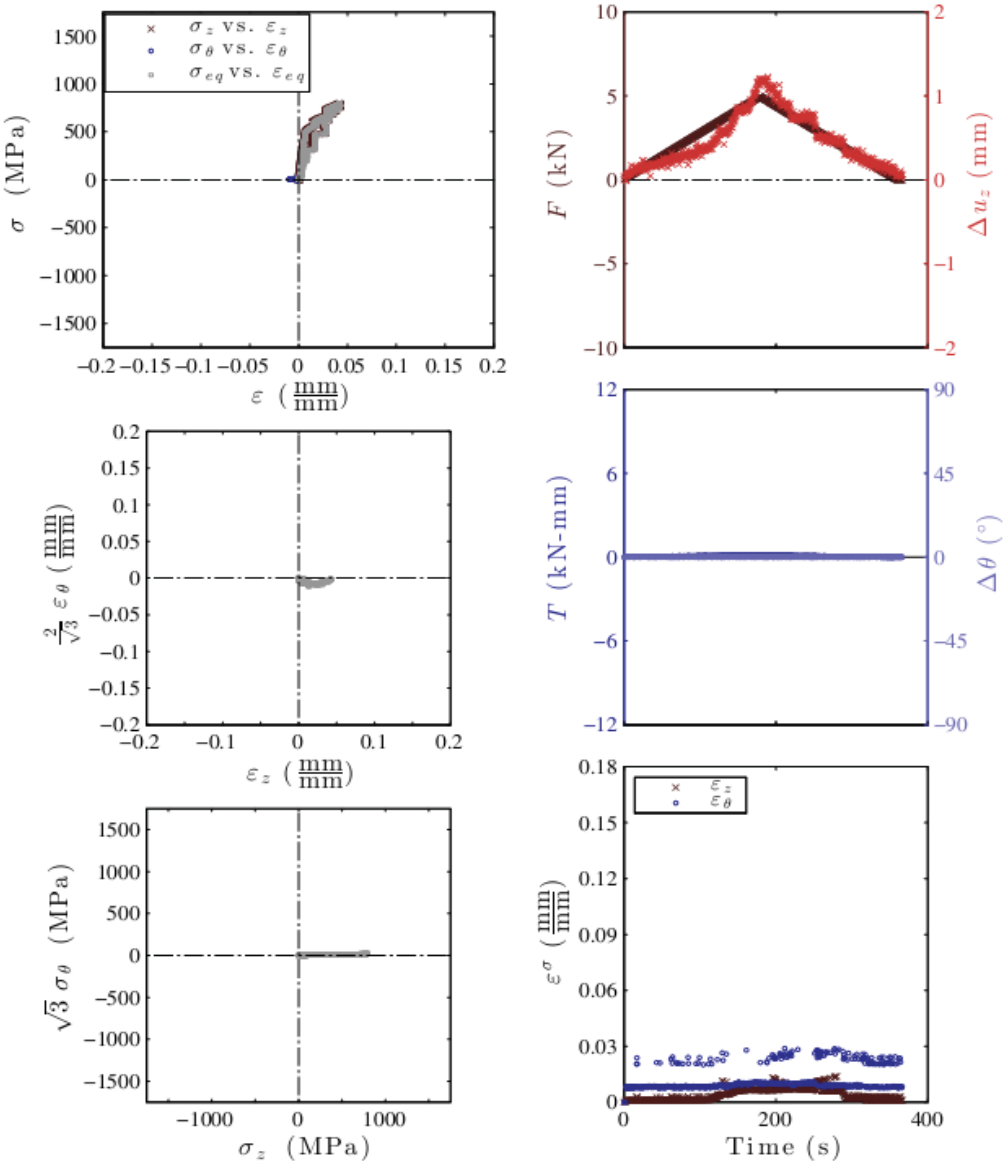

Figure 12.—$Ni_{50.3}Ti_{29.7}Hf_{20}$ Sample 3 responses for test sequence segment no. 3. Type I loading to 4950 N (~0.8 GPa) axial force, 0° rotation control, and temperature maintained at 180 °C.

3.1.3.2 Type III Loading at 180 °C

This data was recorded after three unsuccessful trials due to a grip holder nut that kept breaking loose. Some substantial torque was applied during the failed trials but stress was well below the plastic flow stress. In this test, a bit of slipping of the nut around 6 N-m load was also observed, but it tightened after that for the remainder of the tests. The steps in the stress-strain curve (increase in torque without increase in strain) are from this slippage in the grips and is not a material response.

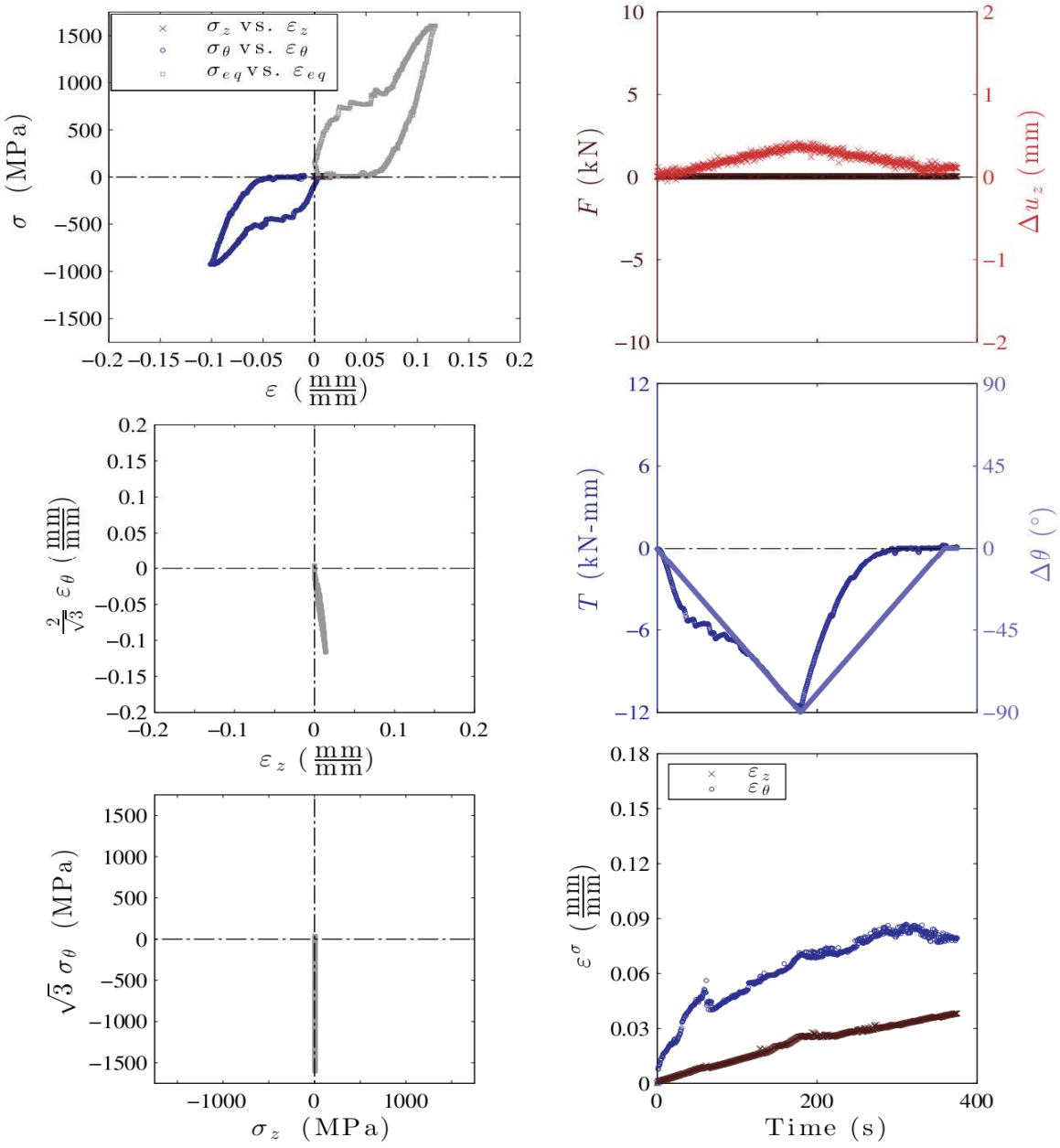

Figure 13.—$Ni_{50.3}Ti_{29.7}Hf_{20}$ Sample 3 responses for test sequence segment no. 4. Type III loading with 0 N axial force, twist to 90° rotation angle, temperature maintained at 180 °C.

3.1.3.3 Type IV Loading at 180 °C

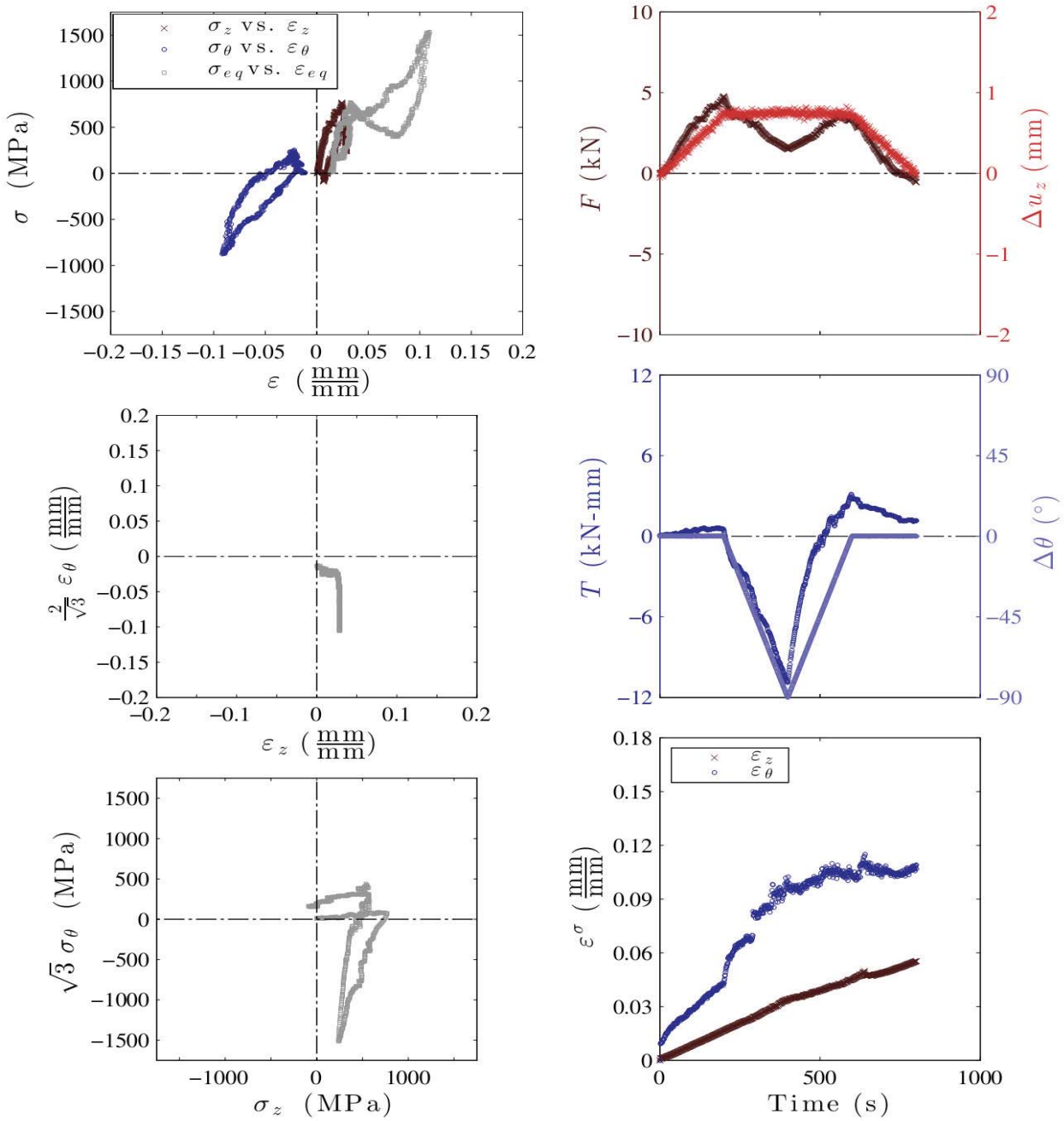

Figure 14.—$Ni_{50.3}Ti_{29.7}Hf_{20}$ Sample 3 responses for test sequence segment no. 5. Type IV loading to an axial displacement corresponding to ~2 percent axial strain, twist to 90° rotation angle, while temperature was maintained at 180 °C.

3.1.3.4 Type V Loading at 180 °C

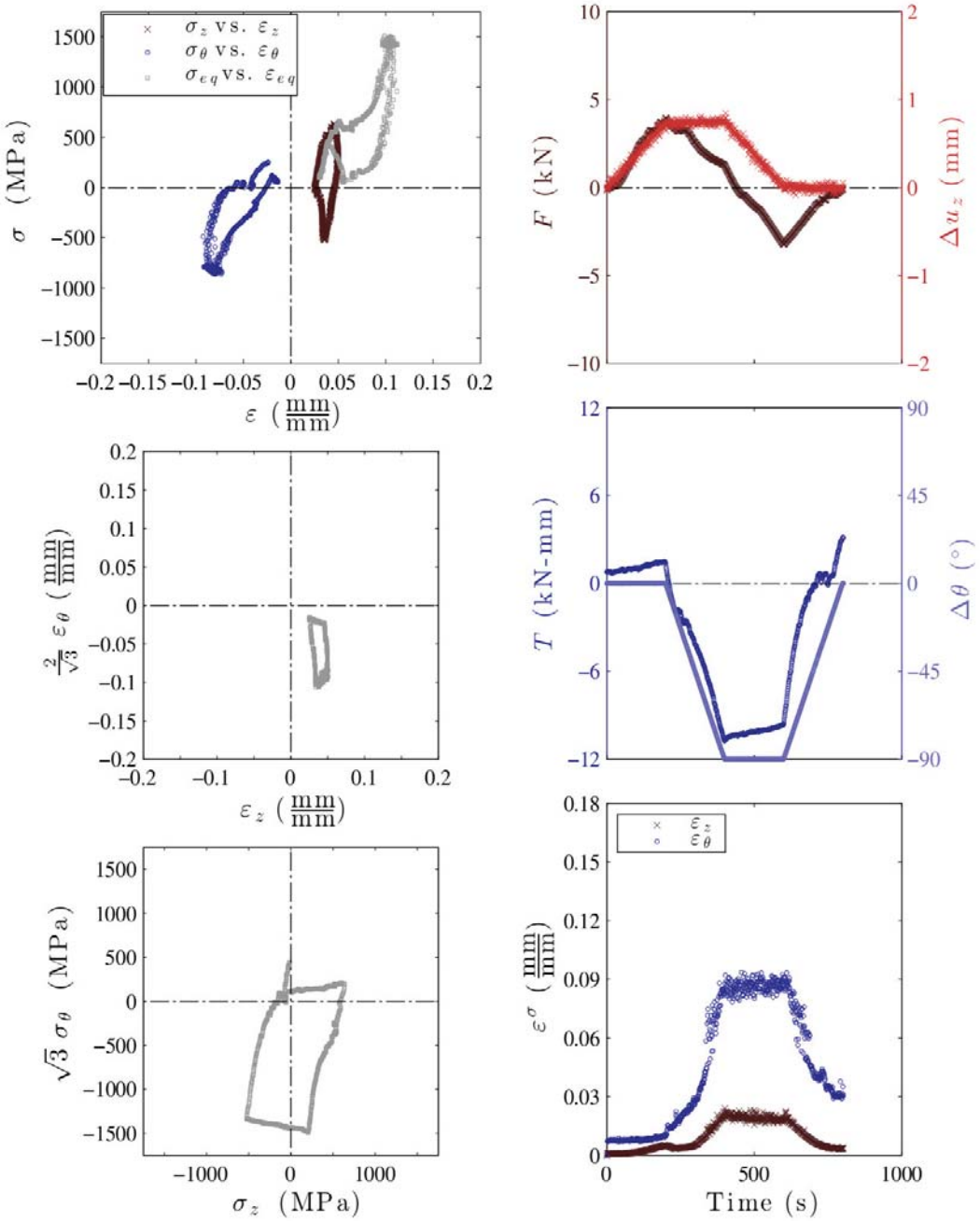

Figure 15.—$Ni_{50.3}Ti_{29.7}Hf_{20}$ Sample 3 responses for test sequence segment no. 6. Type V loading to an axial displacement corresponding to ~2 percent axial strain, twist to 90° rotation angle, while temperature was maintained at 180 °C.

3.1.3.5 Type VI Loading at 180 °C

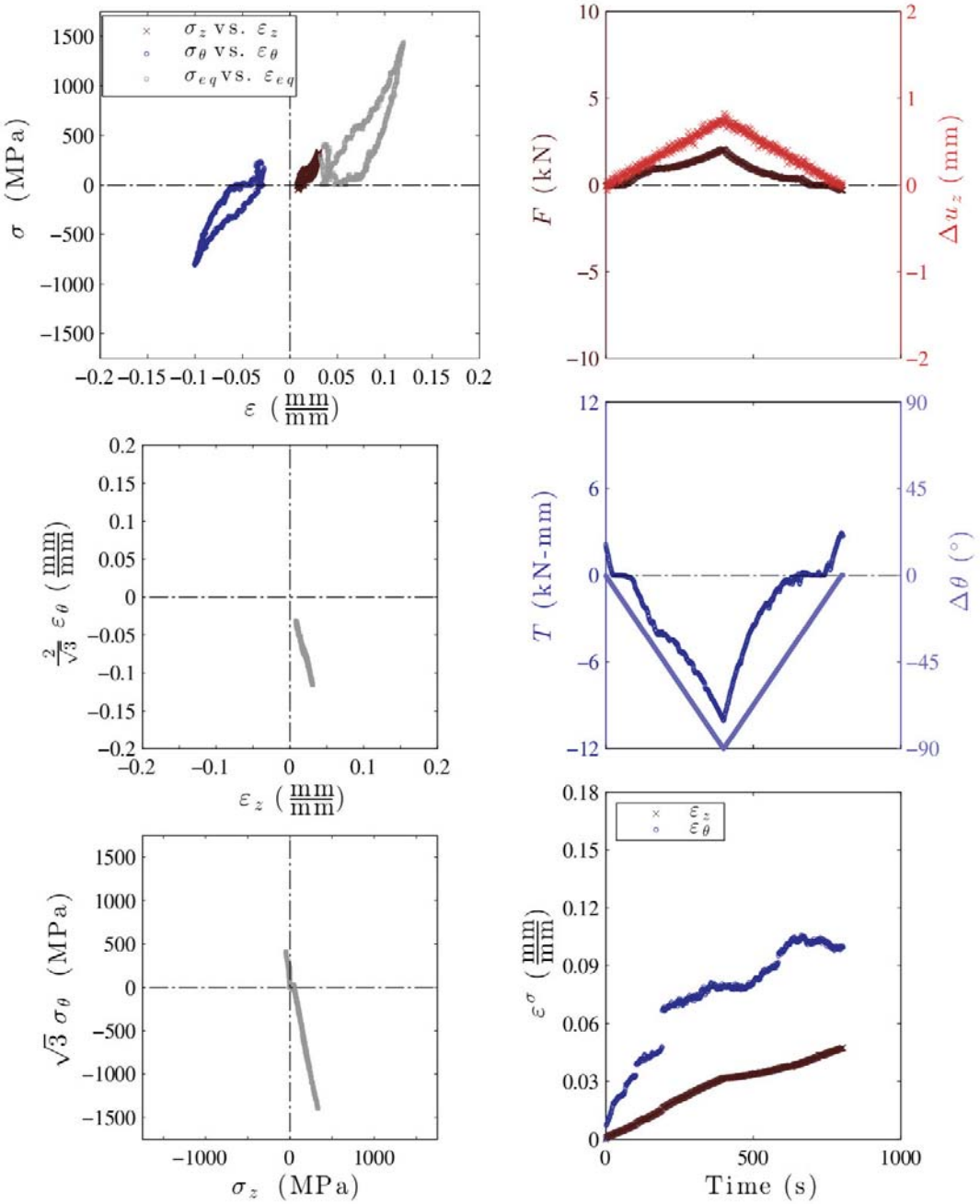

Figure 16.—$Ni_{50.3}Ti_{29.7}Hf_{20}$ Sample 3 responses for test sequence segment no. 7. Type VI loading to an axial displacement corresponding to ~2 percent axial strain, twist to 90° rotation angle, while temperature was maintained at 180 °C.

3.1.3.6 Type I Loading at 220 °C

Before this test segment, the sample was cycled in temperature between 240 °C and RT twice and then heated to 220 °C with crossheads fixed (in both axial and rotation). See Section 2.4.1 for details.

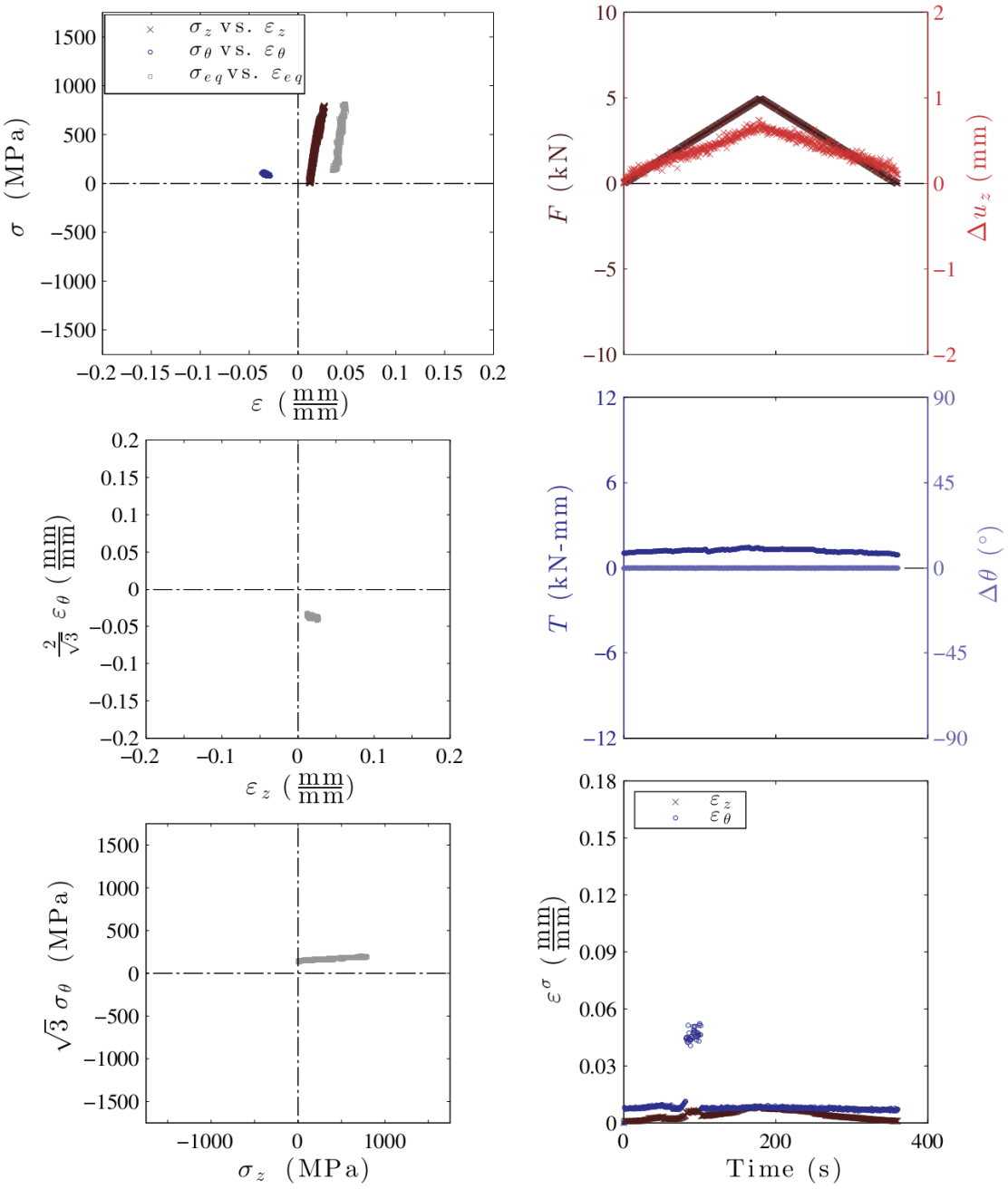

Figure 17.—$Ni_{50.3}Ti_{29.7}Hf_{20}$ Sample 3 responses for test sequence segment no. 10. Type I loading to 4950 N (~0.8 GPa) axial force, 0° rotation control, while temperature maintained at 220 °C.

3.1.3.7 Type III Loading at 220 °C

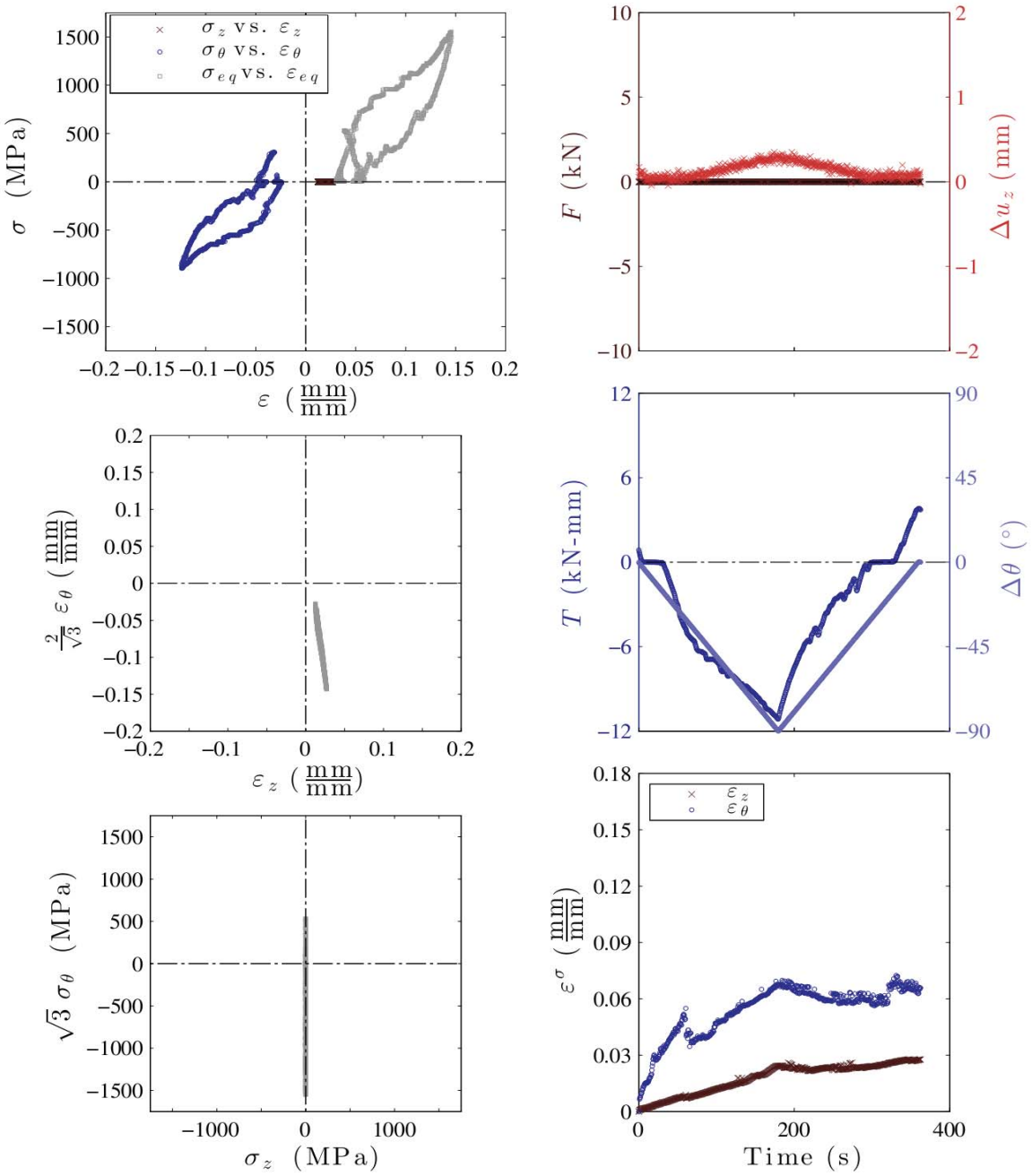

Figure 18.—$Ni_{50.3}Ti_{29.7}Hf_{20}$ Sample 3 responses for test sequence segment no. 11. Type III loading with 0 N axial force, twist to 90° rotation angle, while temperature was maintained at 220 °C.

3.1.3.8 Type VI Loading at 220 °C

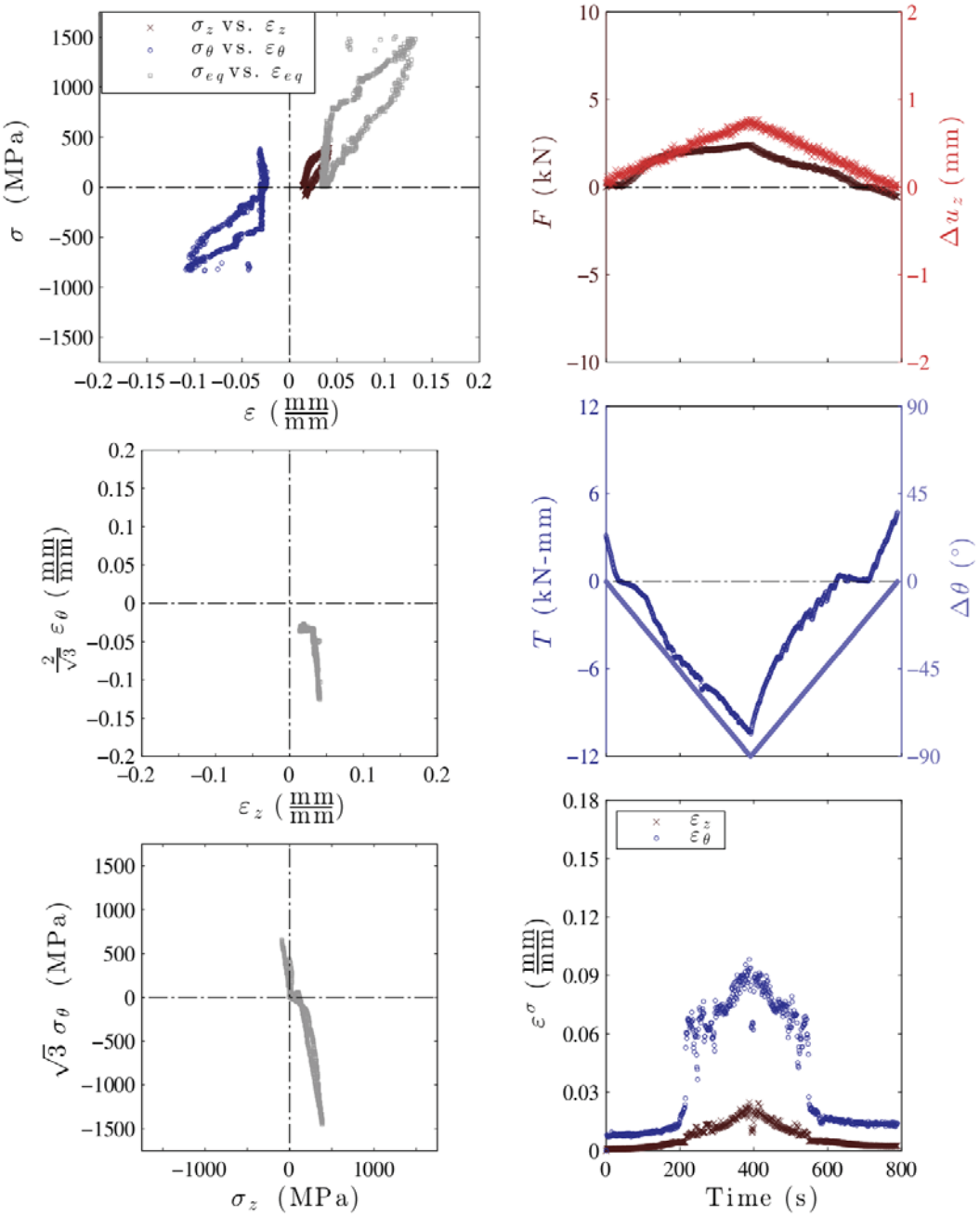

Figure 19.—$Ni_{50.3}Ti_{29.7}Hf_{20}$ Sample 3 responses for test sequence segment no. 12. Type VI loading to an axial displacement corresponding to ~2 percent axial strain, twist to 90° rotation angle, while temperature maintained at 220 °C.

3.1.3.9 Type IV Loading at 220 °C

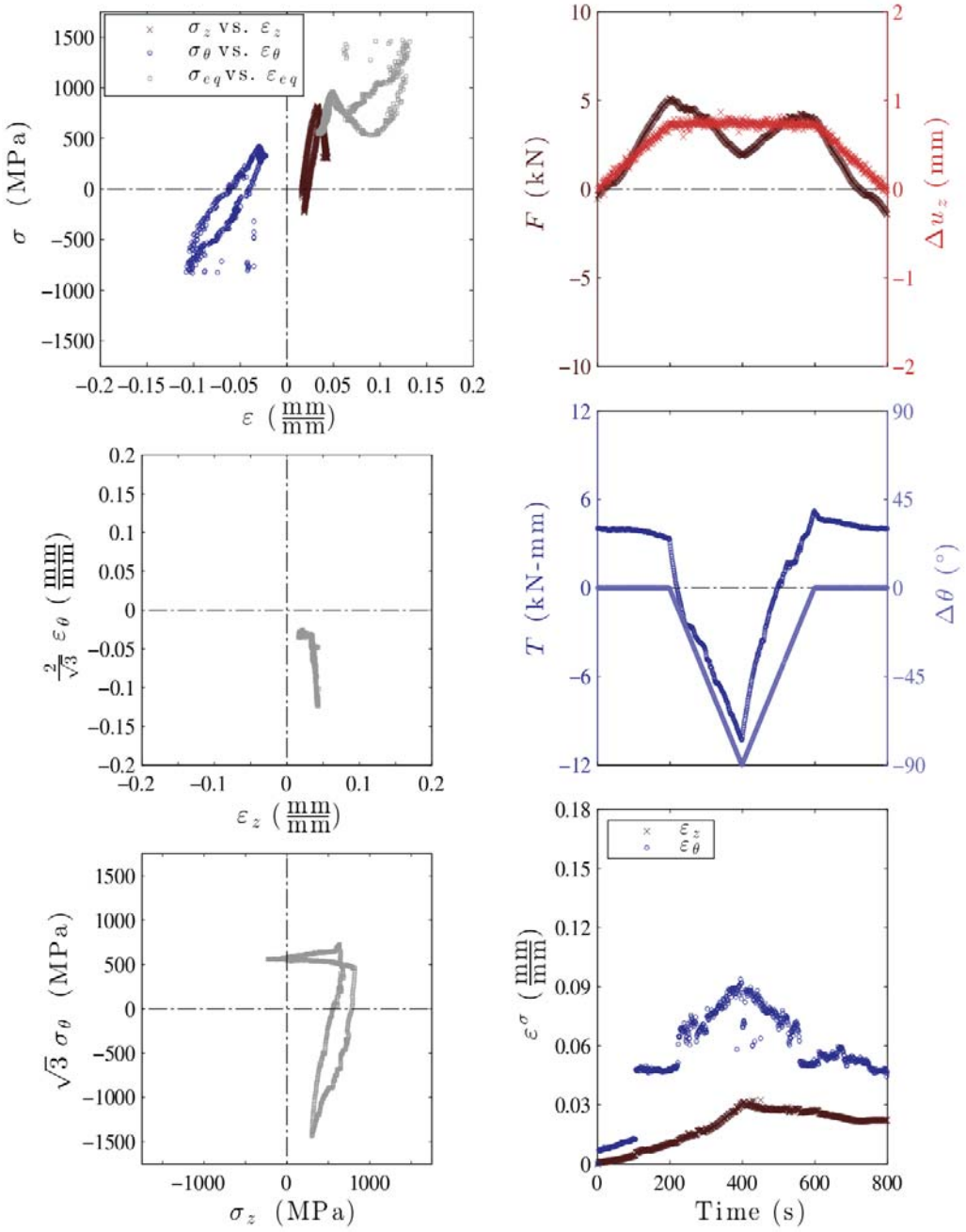

Figure 20.—$Ni_{50.3}Ti_{29.7}Hf_{20}$ Sample 3 responses for test sequence segment no. 13. Type IV loading to an axial displacement corresponding to ~2 percent axial strain, twist to 90° rotation angle, while temperature maintained at 220 °C.

3.1.3.10 Type V Loading at 220 °C

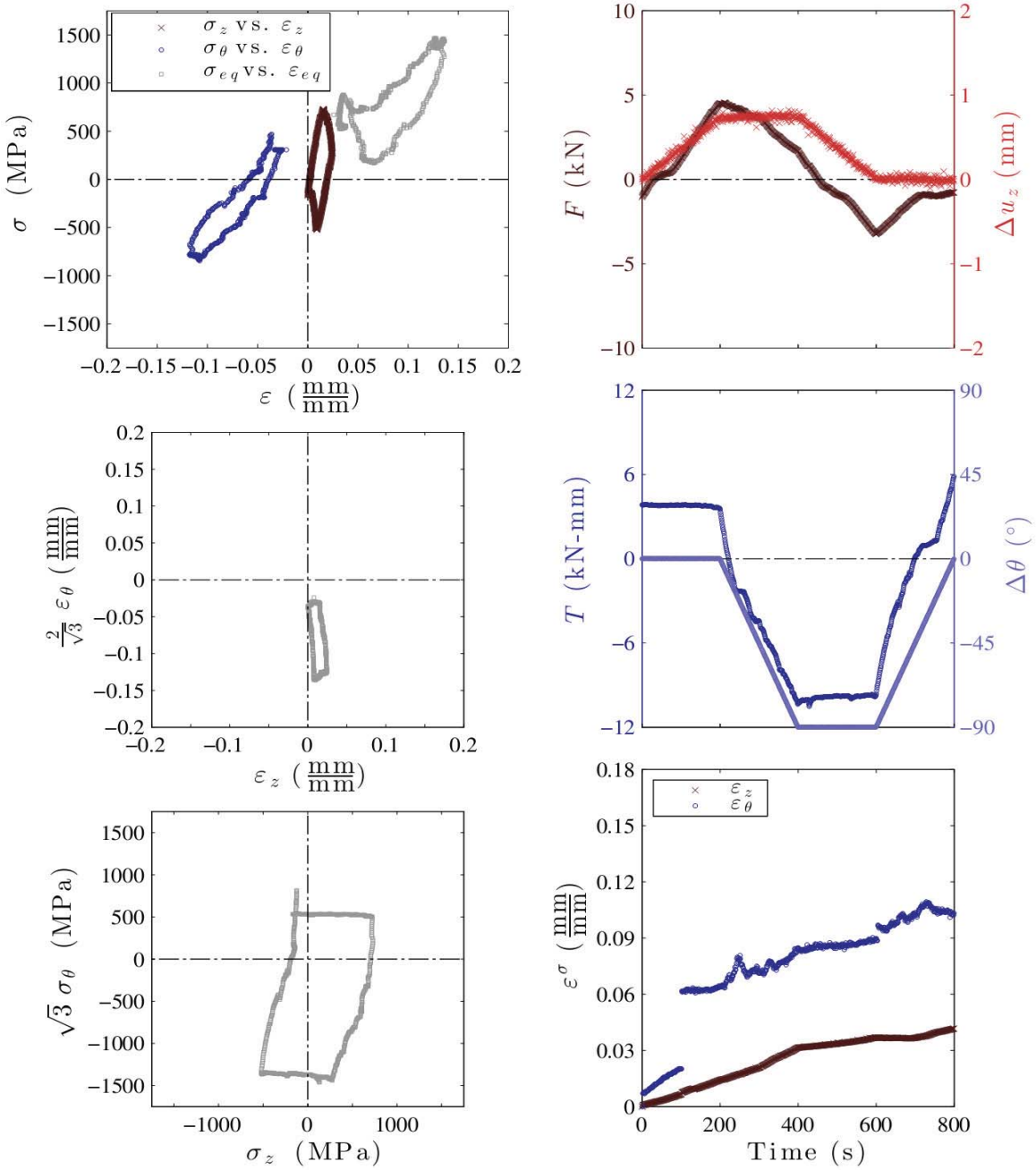

Figure 21.—$Ni_{50.3}Ti_{29.7}Hf_{20}$ Sample 3 responses for test sequence segment no. 14. Type V loading to an axial displacement corresponding to ~2 percent axial strain, twist to 90° rotation angle, while temperature maintained at 220 °C.

3.1.4 Sample 4

This sample was utilized in performing a series of Compression-Torsion experiments at 180 and 220 °C. Refer to Section 2.4.2 for a complete loading history for the sample and for additional details of the various test sequence segments.

3.1.4.1 Type II Loading at 180 °C

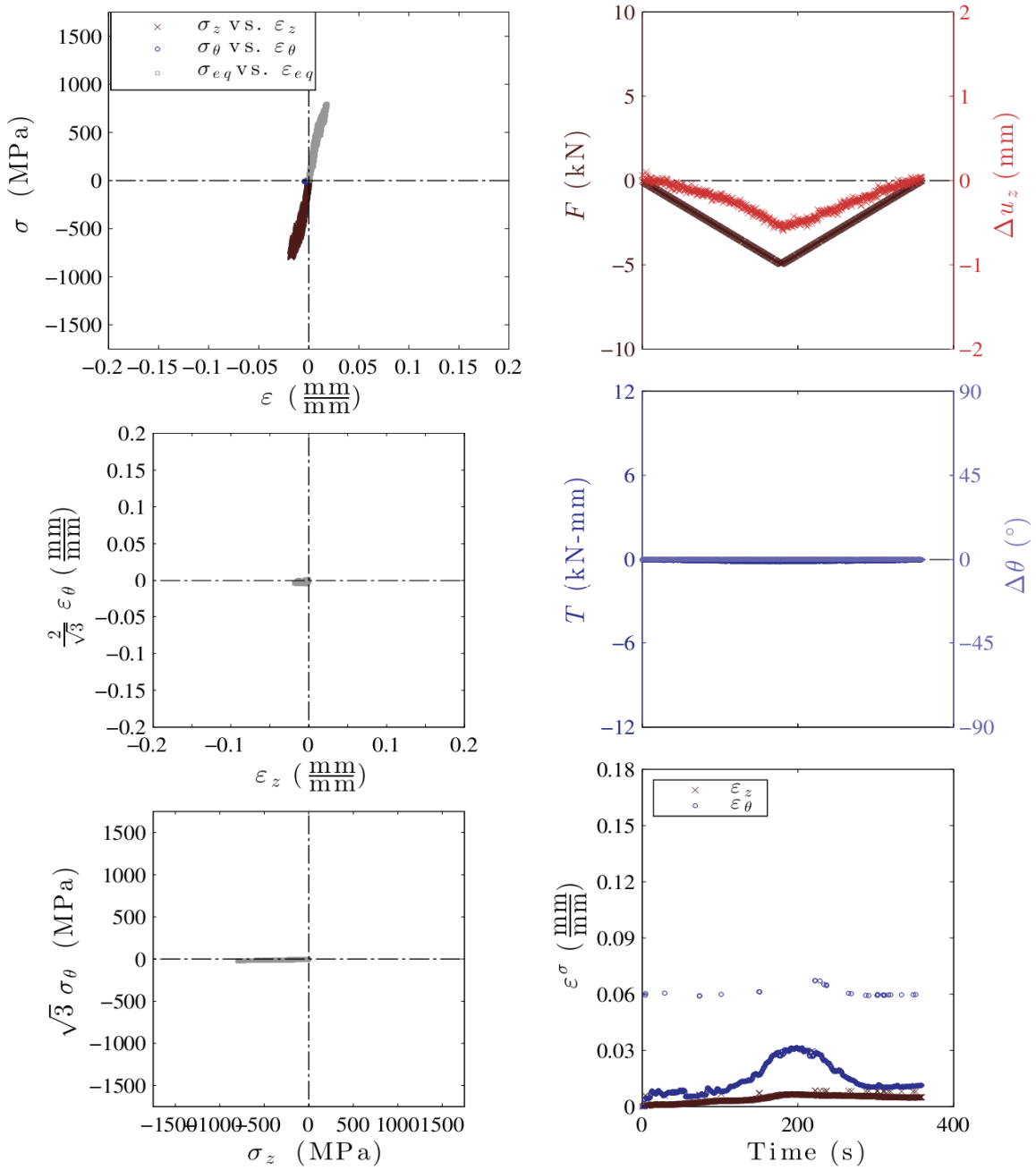

Figure 22.—$Ni_{50.3}Ti_{29.7}Hf_{20}$ Sample 4 responses for test sequence segment no. 3. Type II loading to –4950 N (~–0.8 GPa) axial force, 0° rotation control, while temperature maintained at 180 °C.

3.1.4.2 Type III Loading at 180 °C

This data was recorded after 2 unsuccessful trials due to a grip holder nut breaking loose. Some substantial torque was applied during the failed trials but plastic strain data could not be recorded. However, it was assumed that there were no plastic strains imparted to the sample during the failed trials.

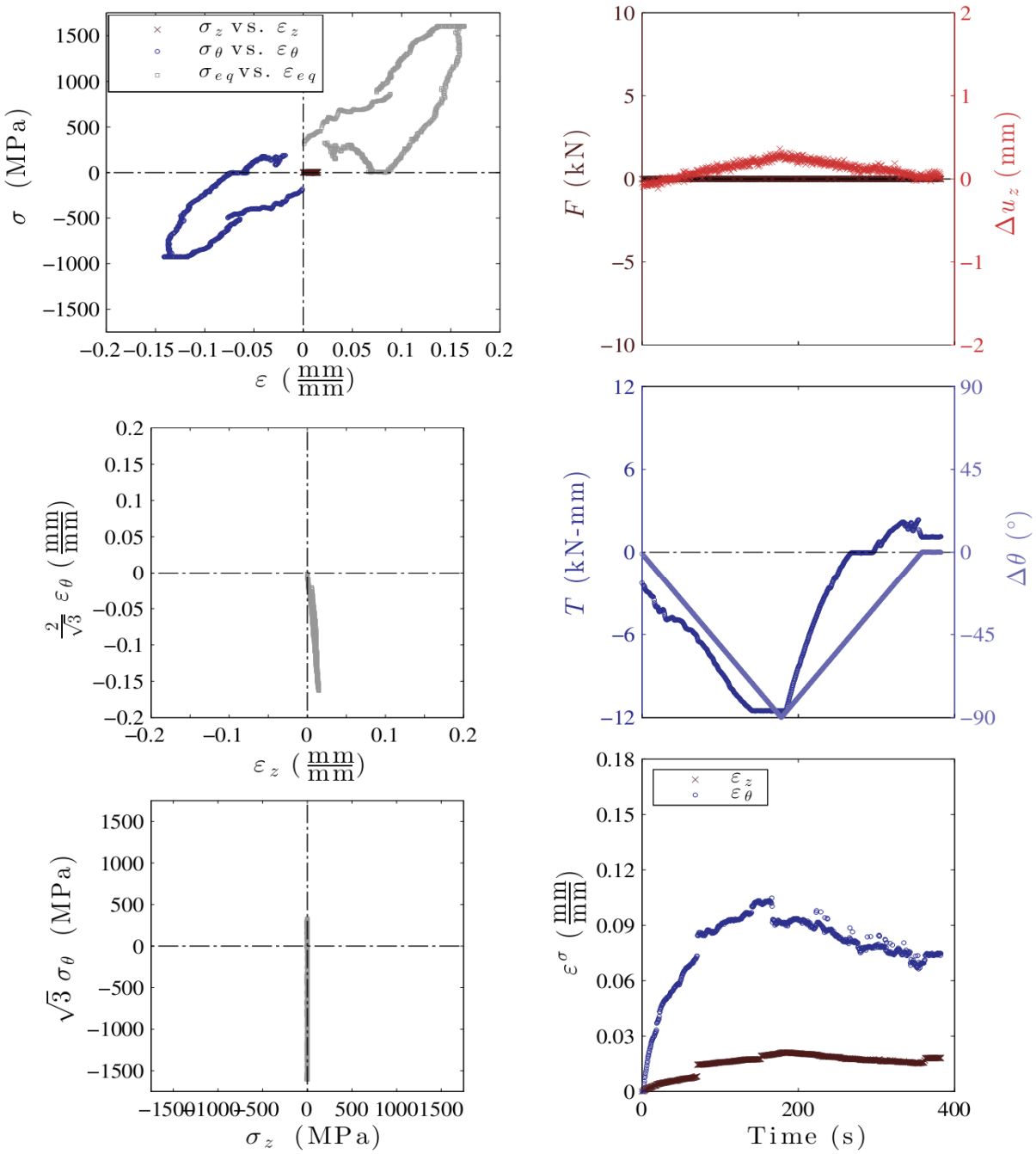

Figure 23.—$Ni_{50.3}Ti_{29.7}Hf_{20}$ Sample 4 responses for test sequence segment no. 4. Type III loading at 0 N axial force, twist to 90° rotation angle, while temperature maintained at 180 °C.

3.1.4.3 Type IV Loading at 180 °C

The initial stress observed in the plots is due to torque introduced to tighten the nut, which broke loose while performing the first attempt at this segment. This residual torque is carried through the remainder of the test segments for this sample.

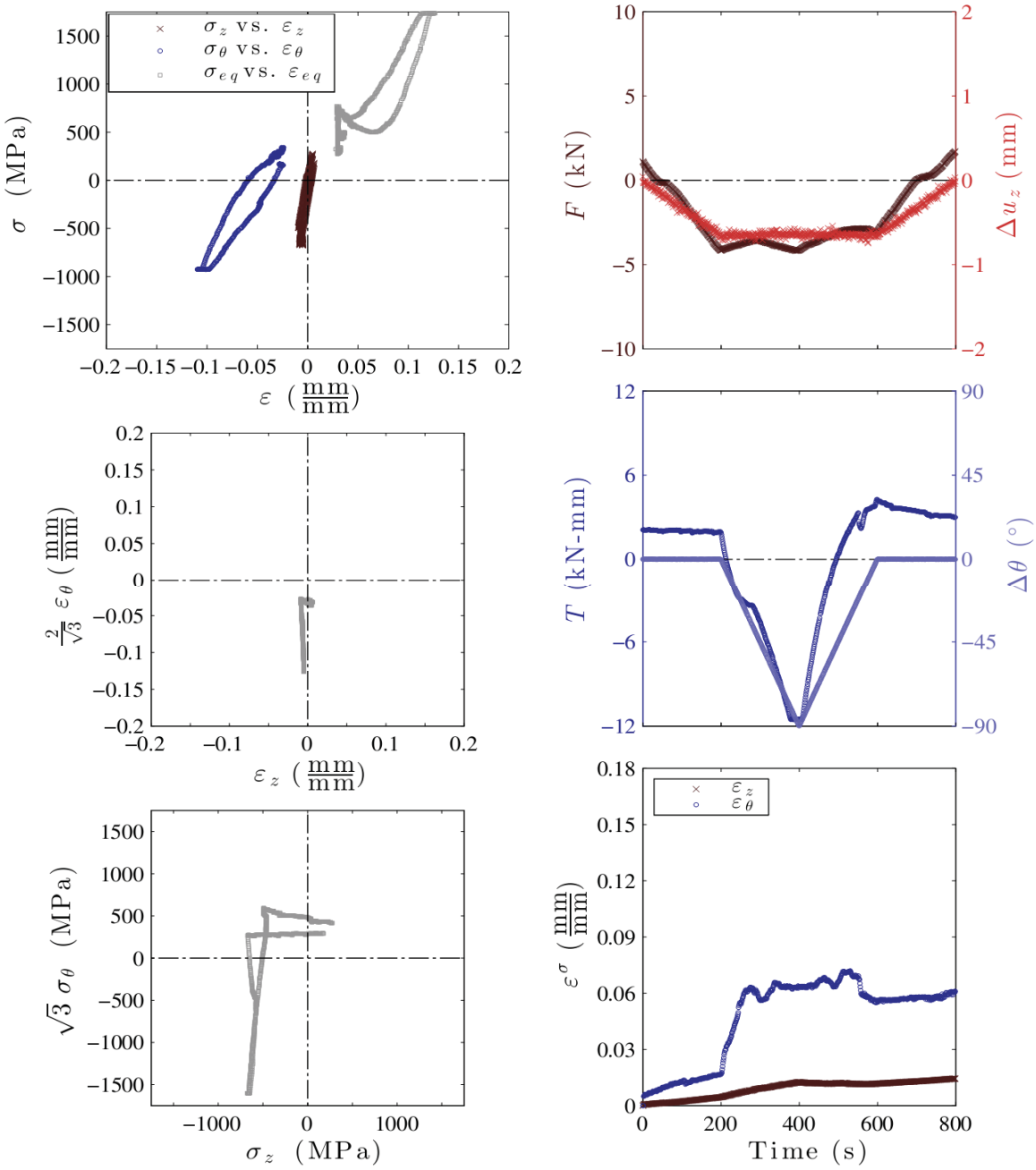

Figure 24.—$Ni_{50.3}Ti_{29.7}Hf_{20}$ Sample 4 responses for test sequence segment no. 5. Type IV loading to an axial displacement corresponding to ~–2 percent axial strain, twist to 90° rotation angle, while temperature maintained at 180 °C.

3.1.4.4 Type V Loading at 180 °C

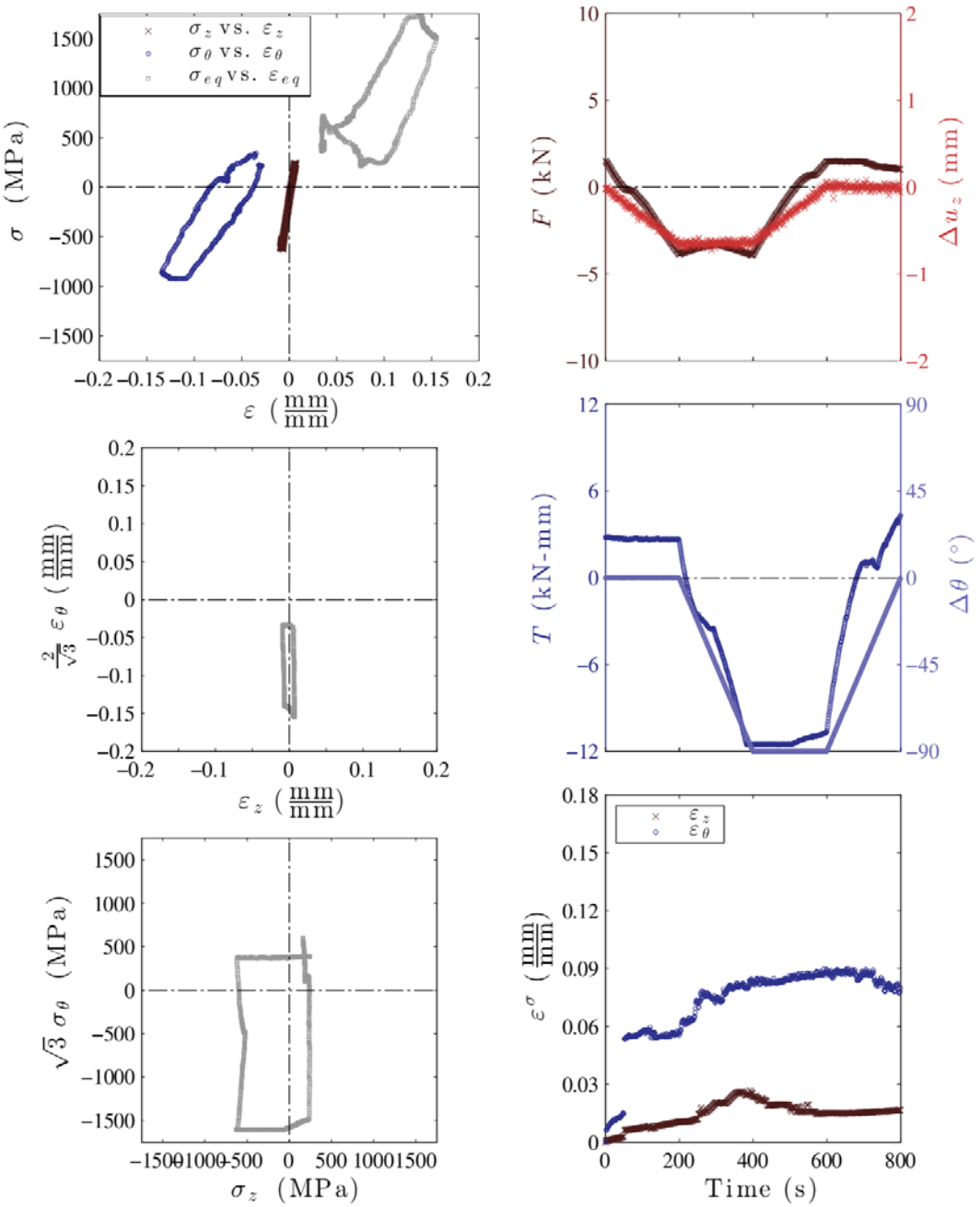

Figure 25.—$Ni_{50.3}Ti_{29.7}Hf_{20}$ Sample 4 responses for test sequence segment no. 6. Type V loading to an axial displacement corresponding to ~–2 percent axial strain, twist to 90° rotation angle, while temperature maintained at 180 °C.

3.1.4.5 Type VI Loading at 180 °C

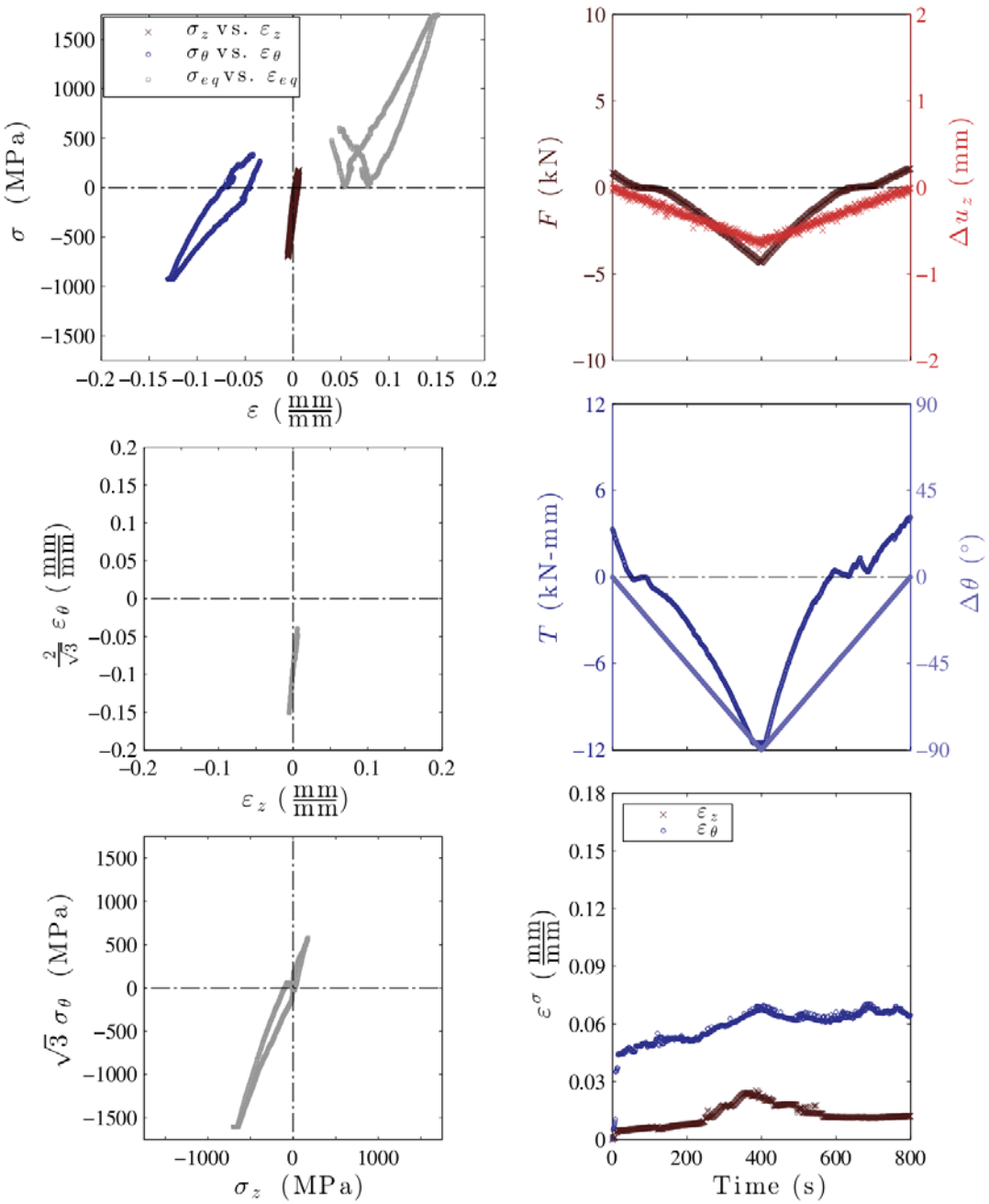

Figure 26.—$Ni_{50.3}Ti_{29.7}Hf_{20}$ Sample 4 responses for test sequence segment no. 7. Type VI loading to an axial displacement corresponding to ~–2 percent axial strain, twist to 90° rotation angle, while temperature maintained at 180 °C.

3.1.4.6 Type II Loading at 220 °C

Before this test, the sample was cycled in temperature between 240 °C and RT twice and then heated to 220 °C with crossheads fixed (in both axial and rotation). For a complete history of the loading sequence segments on this sample, see Section 2.4.2.

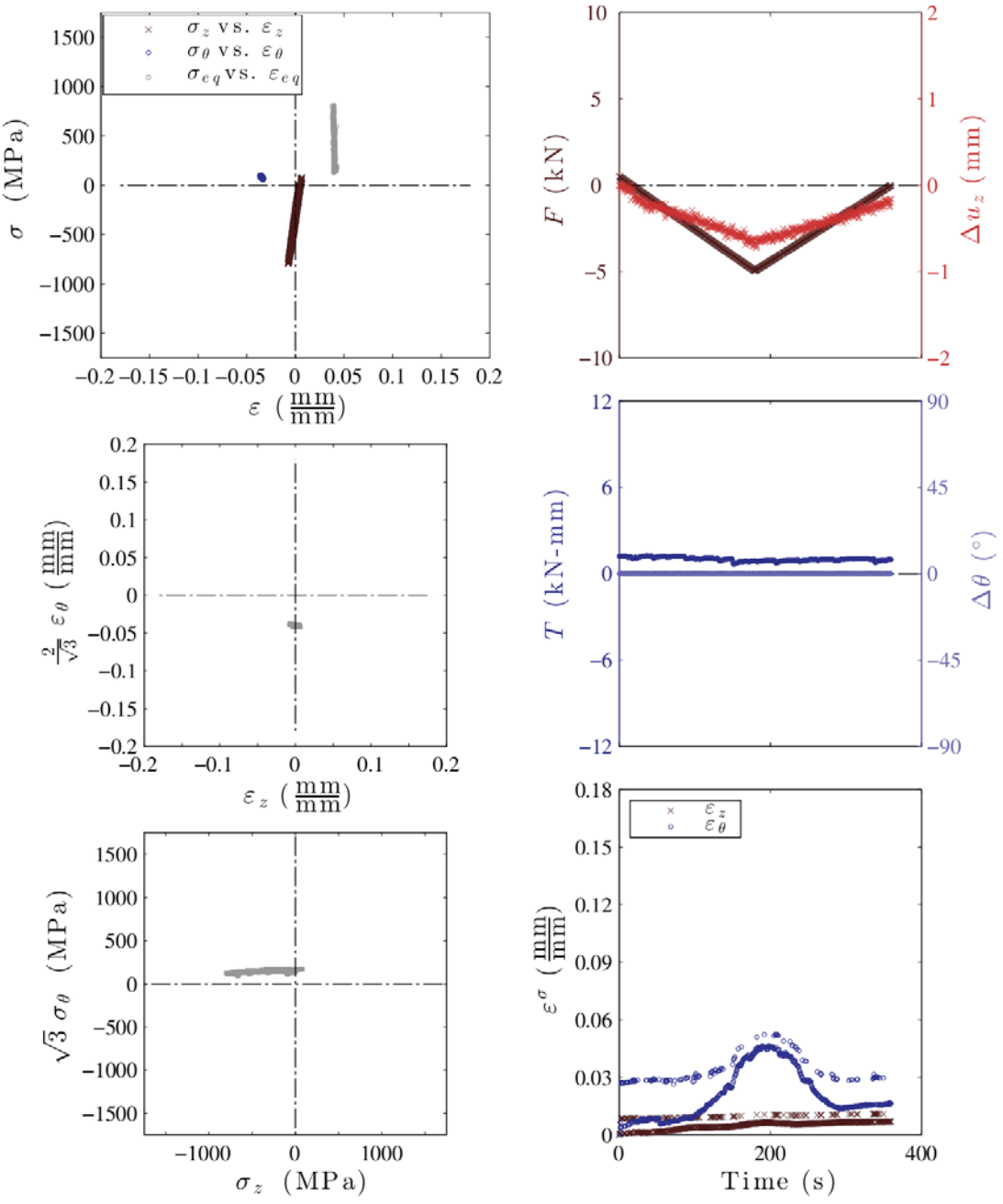

Figure 27.—$Ni_{50.3}Ti_{29.7}Hf_{20}$ Sample 4 responses for test sequence segment no. 10. Type II loading to –4950 N (~–0.8 GPa) axial force, 0° rotation control, while temperature maintained at 220 °C.

3.1.4.7 Type III Loading at 220 °C

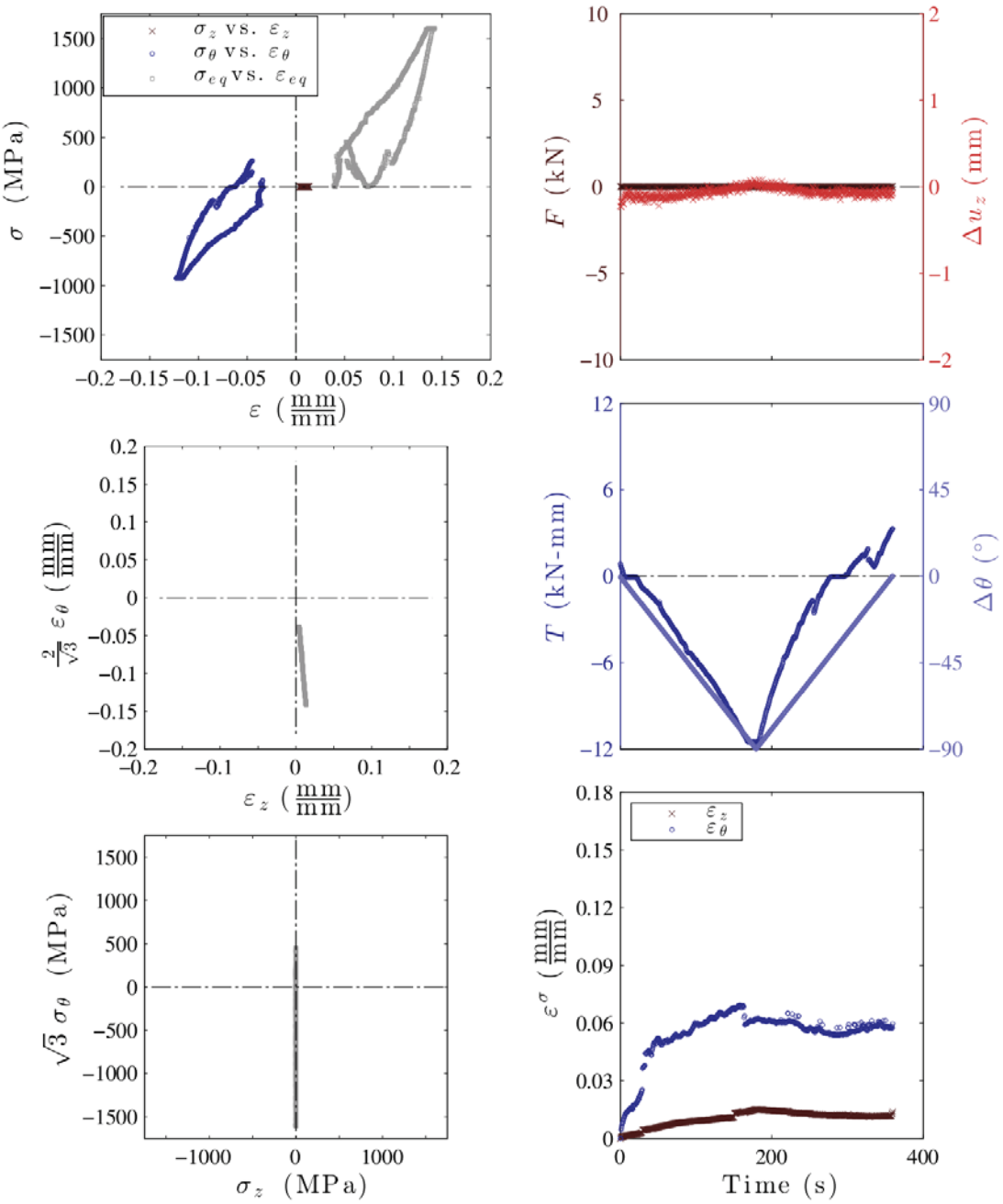

Figure 28.—$Ni_{50.3}Ti_{29.7}Hf_{20}$ Sample 4 responses for test sequence segment no. 11. Type III loading at 0 N axial force, twist to 90° rotation angle, while temperature maintained at 220 °C.

3.1.4.8 Type VI Loading at 220 °C

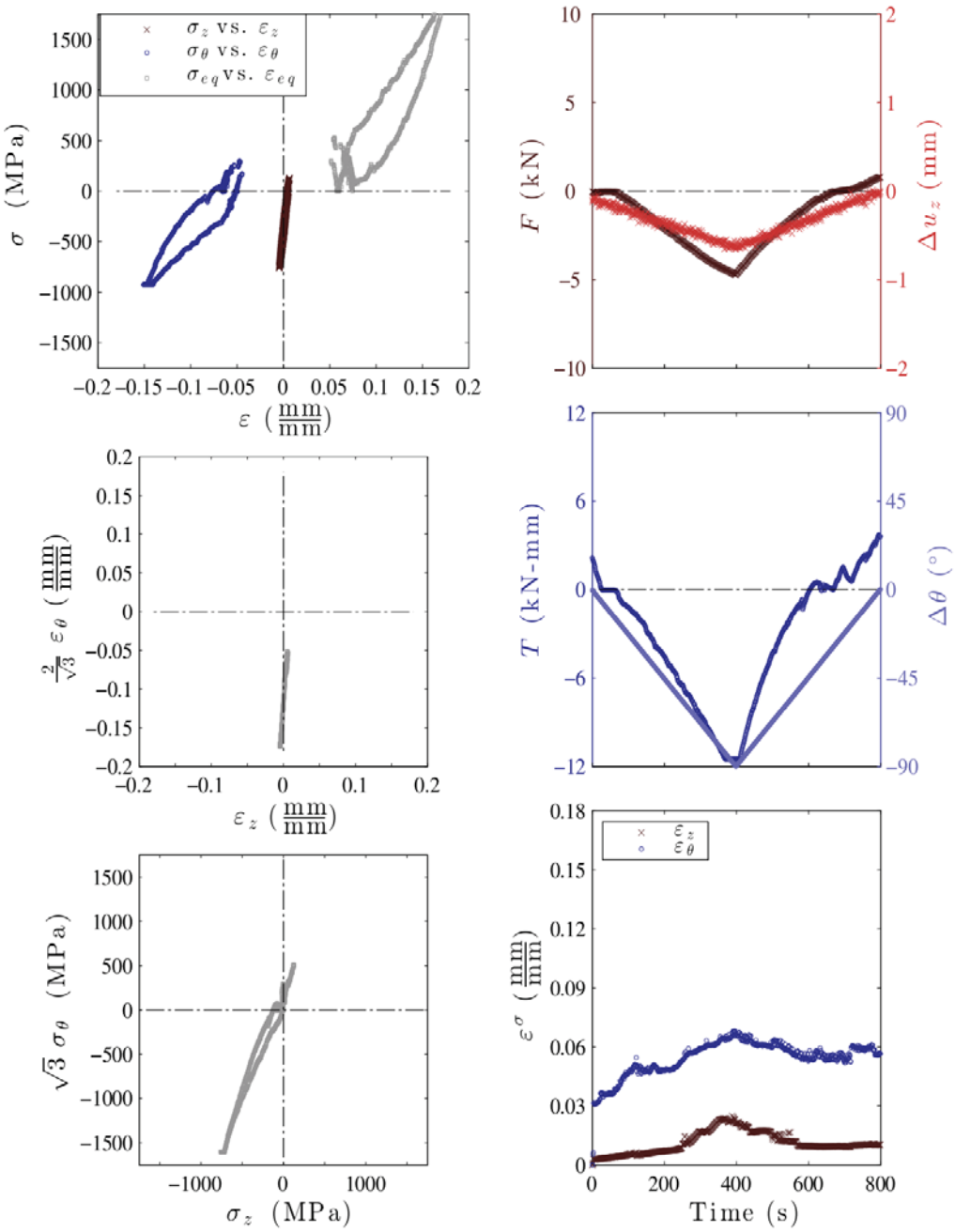

Figure 29.—$Ni_{50.3}Ti_{29.7}Hf_{20}$ Sample 4 responses for test sequence segment no. 12. Type VI loading to an axial displacement corresponding to ~–2 percent axial strain, twist to 90° rotation angle, while temperature maintained at 220 °C.

3.1.4.9 Type V Loading at 220 °C

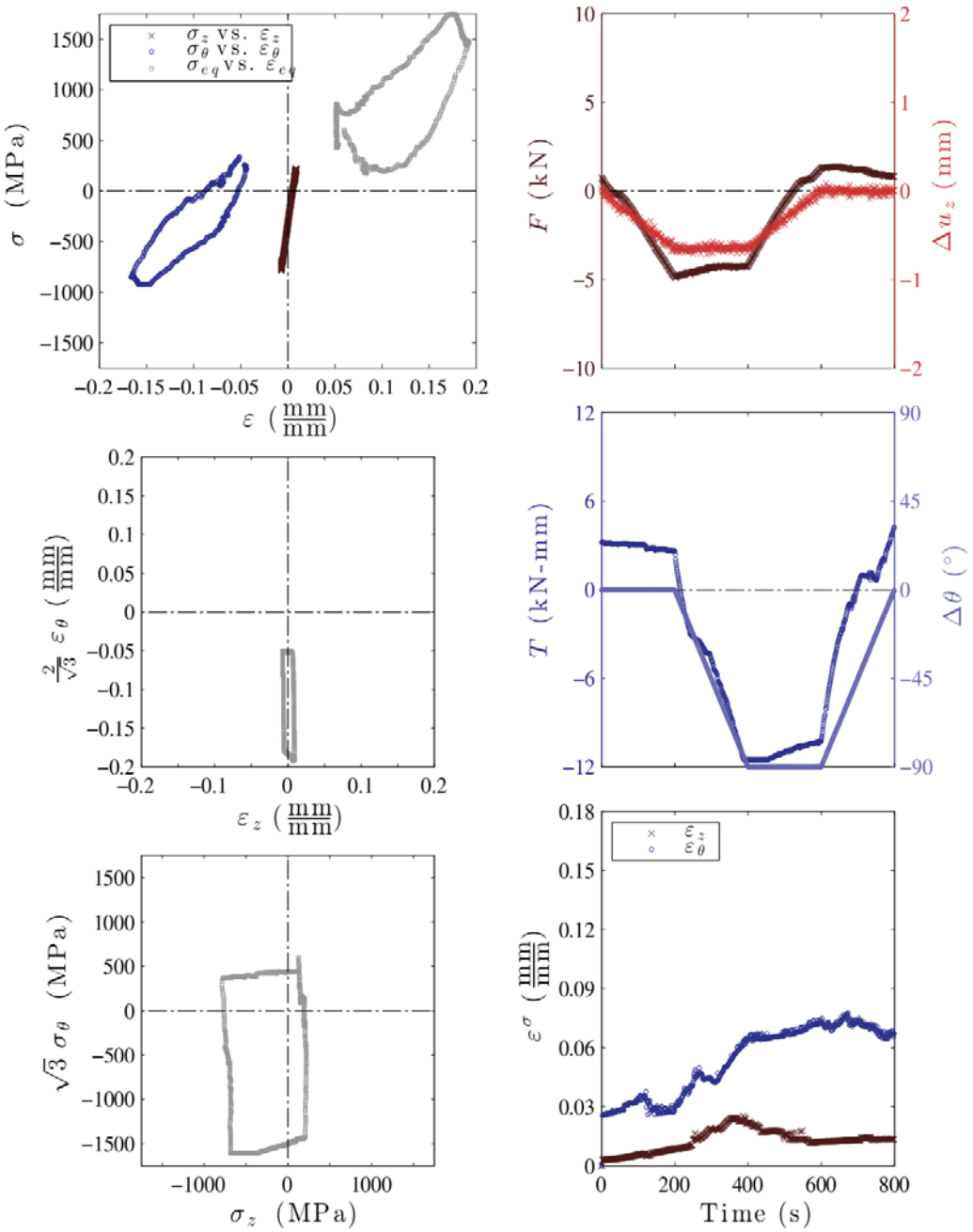

Figure 30.—$Ni_{50.3}Ti_{29.7}Hf_{20}$ Sample 4 responses for test sequence segment no. 13. Type V loading to an axial displacement corresponding to ~–2 percent axial strain, twist to 90° rotation angle, while temperature maintained at 220 °C.

3.1.4.10 Type IV Loading at 220 °C

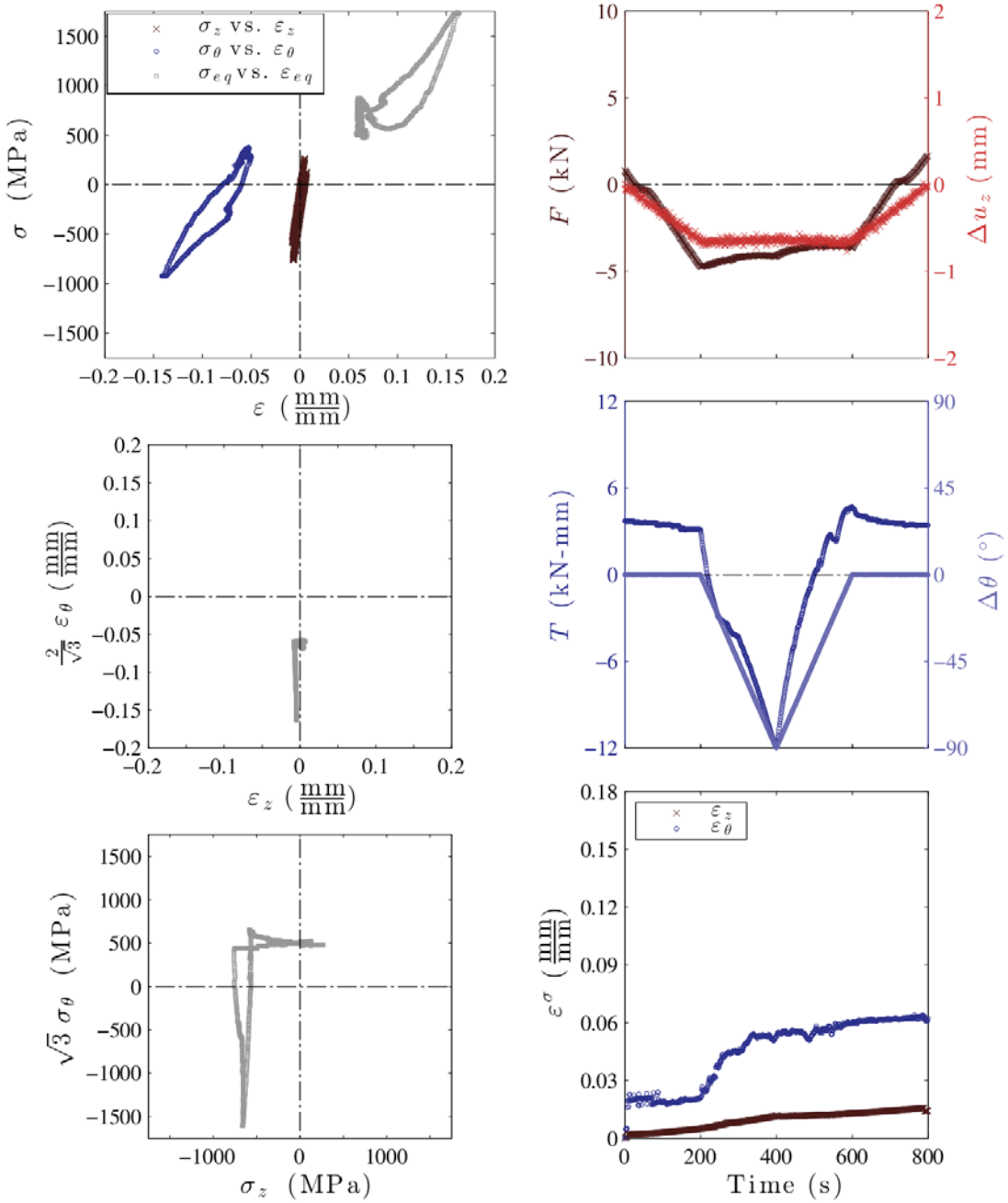

Figure 31.—$Ni_{50.3}Ti_{29.7}Hf_{20}$ Sample 4 responses for test sequence segment no. 14. Type IV loading to an axial displacement corresponding to ~–2 percent axial strain, twist to 90° rotation angle, while temperature maintained at 220 °C.

3.2 $Ni_{50.3}Ti_{33.7}Hf_{16}$ Alloy Experimental Data

The experimental results for the $Ni_{50.3}Ti_{33.7}Hf_{16}$ alloy samples are grouped and presented in the order of the loading types described in Section 2.3.2 in the subsections that follow.

3.2.1 Type A Loading

Type A loading segments (defined in Section 2.3.3) were performed on Samples 1, 2, and 3 (the complete test history for each sample is described in Section 2.5). Figure 32 includes plots of Type A loading tests on Sample 1. The plots for –200, –400, 100, and 200 MPa are shifted in strain because the extensometer was disturbed after the –100 MPa thermal cycle. Thus, these plots can be used to refer quantitatively only to determination of the phase transformation temperatures. Data for Samples 2 and 3 are contained in Figures 33 and 34, respectively, while comparisons of the isobaric thermomechanical response of Samples 2 and 3 are shown in Figures 35 to 37.

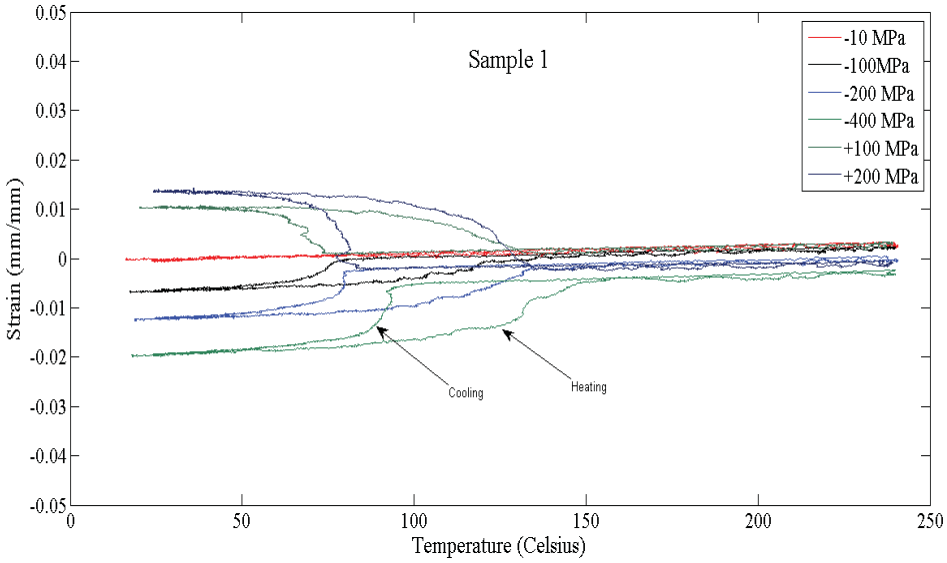

Figure 32.—Thermomechanical responses of $Ni_{50.3}Ti_{33.7}Hf_{16}$ alloy Sample 1 when subjected to Type A loading segments.

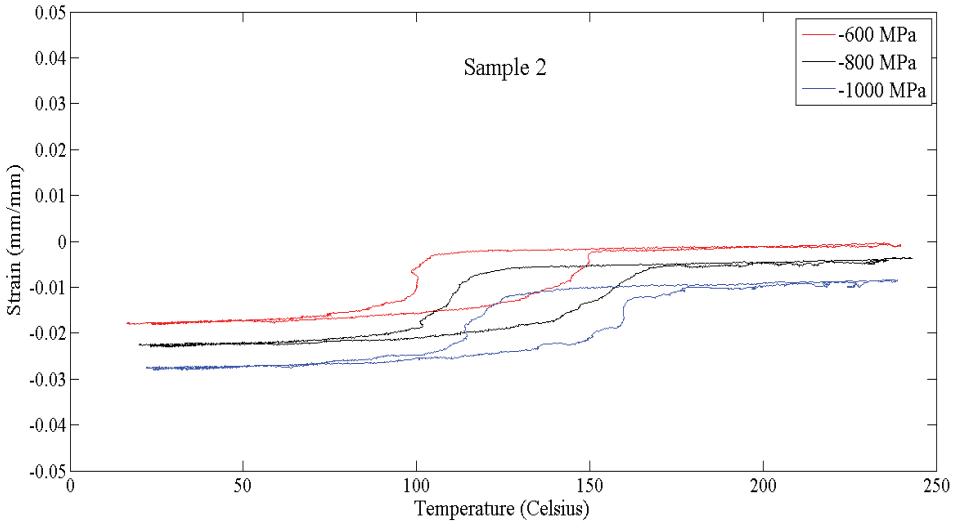

Figure 33.—Thermomechanical responses of $Ni_{50.3}Ti_{33.7}Hf_{16}$ alloy Sample 2 when subjected to Type A loading segments.

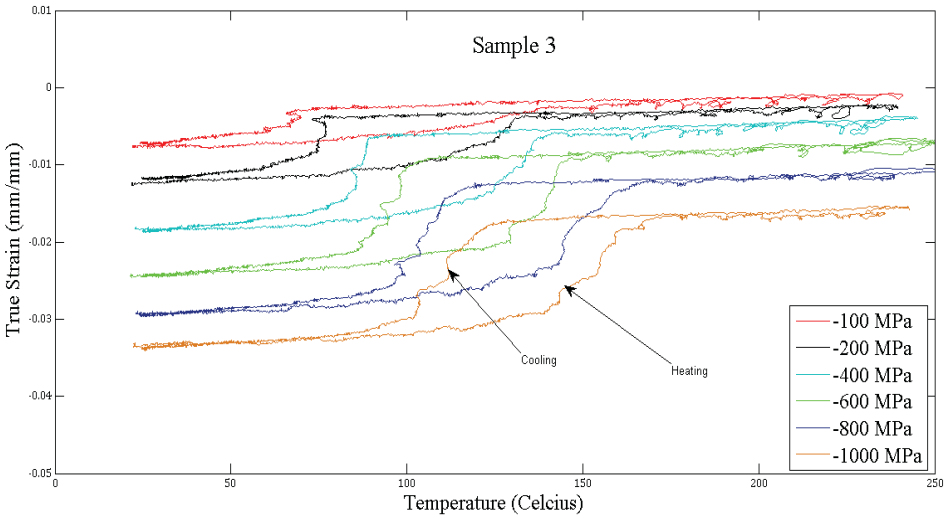

Figure 34.—Thermomechanical responses of $Ni_{50.3}Ti_{33.7}Hf_{16}$ alloy Sample 3 when subjected to Type A loading segments over a broad range of compressive stress.

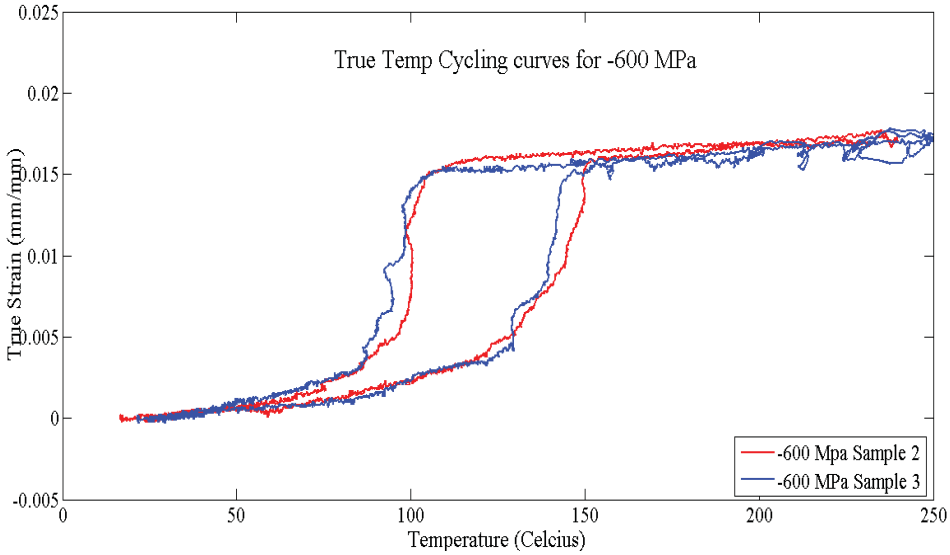

Figure 35.—Comparison of the responses of $Ni_{50.3}Ti_{33.7}Hf_{16}$ alloy Samples 2 and 3 subjected to Type A loading to –7729 N force (–600 MPa) for determining reproducibility of the test results and stability and history dependence of the material to various loading programs.

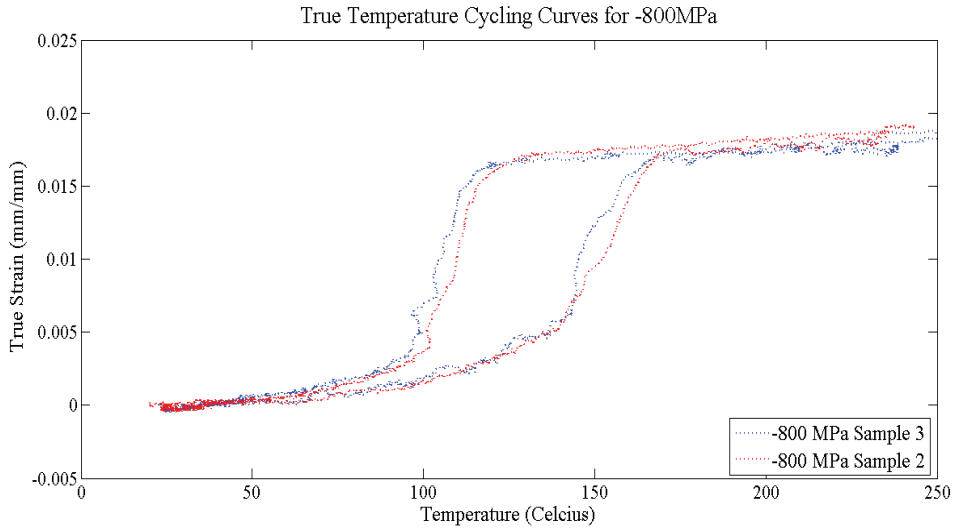

Figure 36.—Comparison of responses of $Ni_{50.3}Ti_{33.7}Hf_{16}$ alloy Samples 2 and 3 subjected to Type A loading to –10306 N force (–800 MPa) for determining reproducibility of the test results and stability and history dependence of the material to various loading programs.

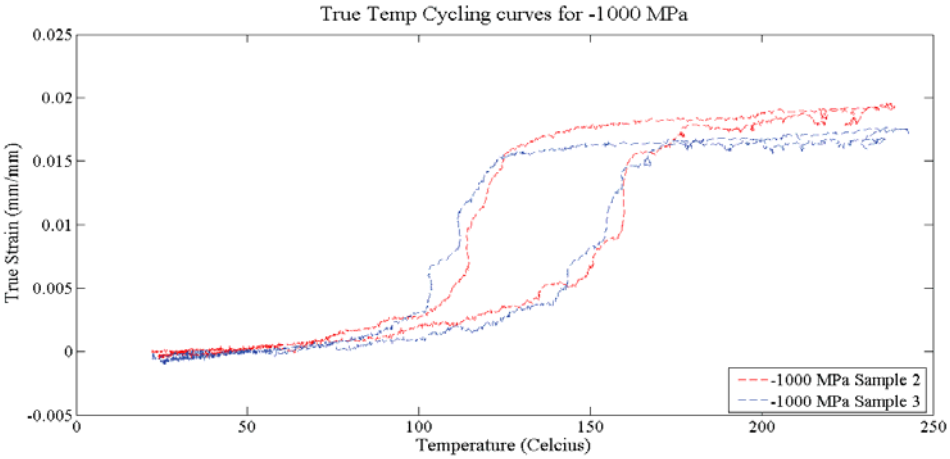

Figure 37.—Comparison of responses of $Ni_{50.3}Ti_{33.7}Hf_{16}$ alloy Samples 2 and 3 subjected to Type A loading to –12882 N force (–1000 MPa) for determining reproducibility of the test results and stability and history dependence of the material to various loading programs.

3.2.2 Type B Loading

Type B loading segments were performed on Samples 2, 3, 4, 5, and 7. In Figure 38, the strain is proportional to stress at temperatures of 150 and 160 °C indicating that the yield strength for the material is above 1 GPa at these temperatures and also indicating that there is no phase transformation (from austenite to martensite) at least for stresses below 1 GPa. It is possible that at these temperatures, the stress-induced transformation could still occur at higher stress levels, assuming that plastic deformation does not occur first. The tests at room temperature were performed without any prior thermal cycling at zero stress (for resetting the alloy). Hence, the curve for the 13000 N force test starts very near the end of the curve for the 12000 N force test, which was performed immediately before it. The legend sequence in Figure 38 appears in the same order as the actual loading sequence for this sample.

Figure 39 shows Type B loading segments on Sample 3 at –600, –800 and –1000 MPa. The tests were performed after completing Type A loading segments (as shown in Fig. 34). A complete loading history for Sample 3 is described in Section 2.5.3. The curve corresponding to –600 MPa load starts from a strain value different from the plots corresponding to –800 and –1000 MPa because the sample had a history of strain, which was reset (heating to 240 °C and back to room temperature at 0 MPa stress) after the loading sequence to –600 and –800 MPa.

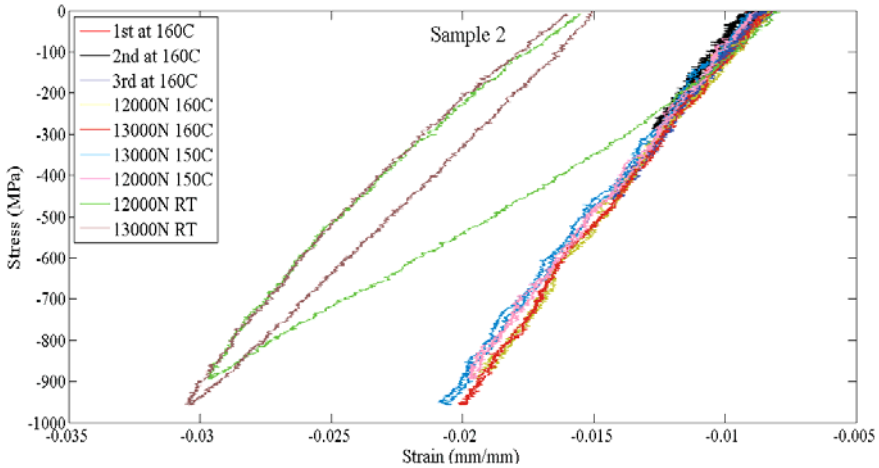

Figure 38.—Stress-strain responses of $Ni_{50.3}Ti_{33.7}Hf_{16}$ alloy Sample 2 subjected to Type B loading segments.

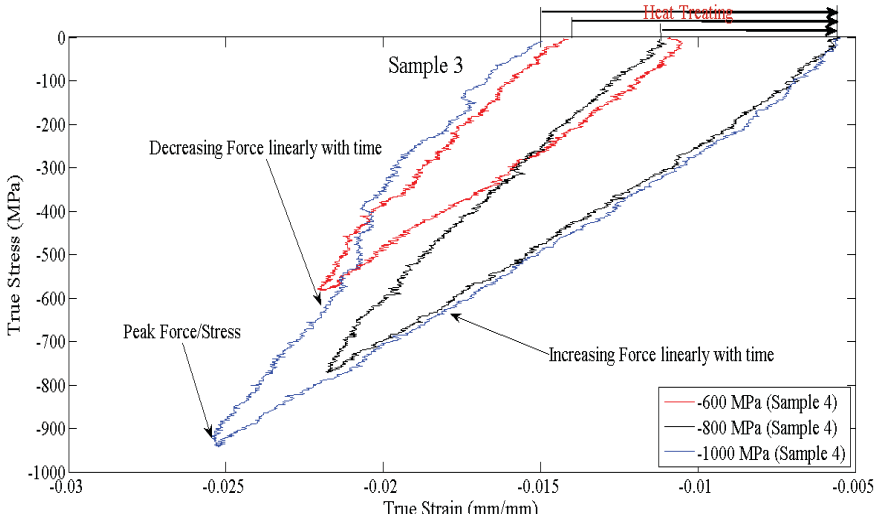

Figure 39.—Stress-strain responses of $Ni_{50.3}Ti_{33.7}Hf_{16}$ alloy Sample 3 subjected to Type B loading segments.

Figure 40 shows Type B loading segments on a virgin, as-received sample (Sample 4), which did not have any thermomechanical cycles prior to testing. The plot for –600 MPa starts at 0 strain but recovers to a different strain value after unloading and stress free thermal cycling. This is presumably due to residual strain introduced during processing and machining of the original material. To check if this was the case, Sample 5 was also loaded similarly, with the only difference that it was temperature cycled to 240 °C and back at 0 MPa twice before loading to –600 MPa. The results (Fig. 41) seem to confirm that the offset observed in the case of Sample 4 was due to residual stress in the as-processed sample.

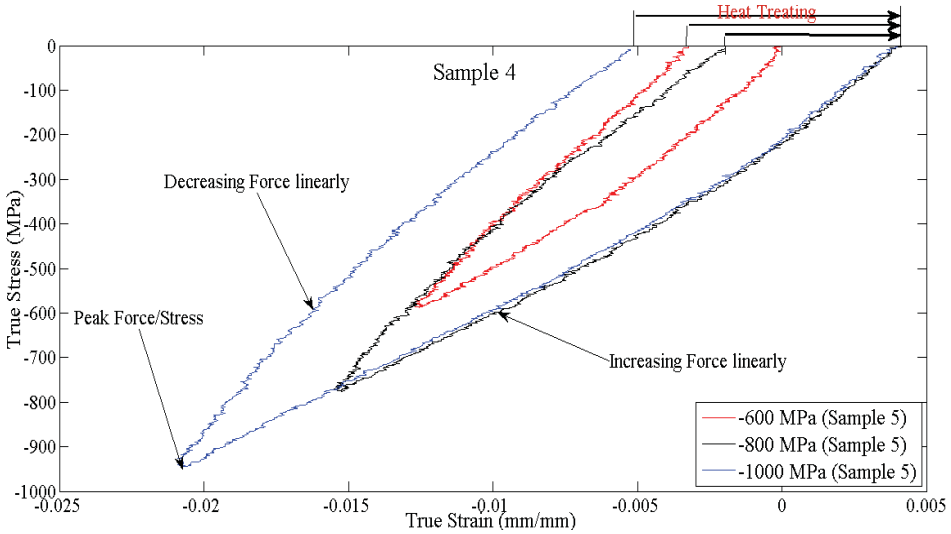

Figure 40.—Stress-strain responses of $Ni_{50.3}Ti_{33.7}Hf_{16}$ alloy Sample 4 subjected to Type B loading segments.

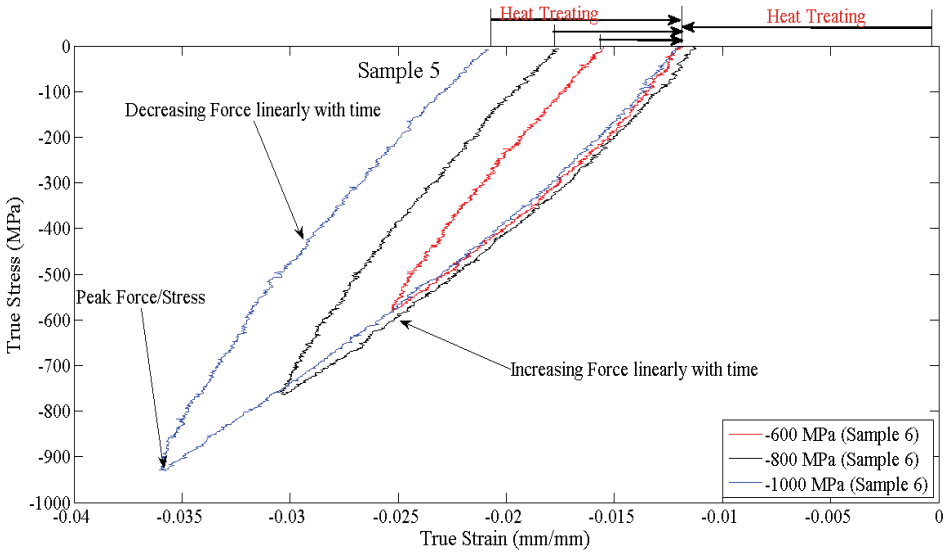

Figure 41.—Stress-strain responses of $Ni_{50.3}Ti_{33.7}Hf_{16}$ alloy Sample 2 subjected to Type B loading segments.

Figures 42 to 44 provide a measure of the reproducibility of the test data at a particular stress level, given the large difference in loading history for each sample. Data for Samples 4 and 5 were more consistent than that for Sample 3, which underwent a significant number of Type A loading events prior to the isothermal deformations (Type B loading).

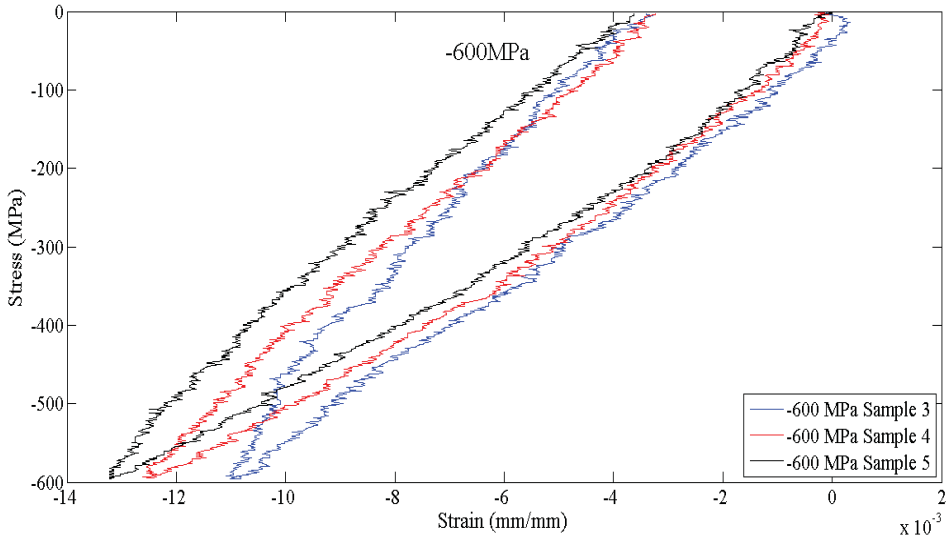

Figure 42.—Comparison of the responses for $Ni_{50.3}Ti_{33.7}Hf_{16}$ alloy Samples 3 to 5 subjected to Type B loading to –7729 N force (–600 MPa) for determination of the reproducibility of the test data and stability of the material (initial strains adjusted to zero).

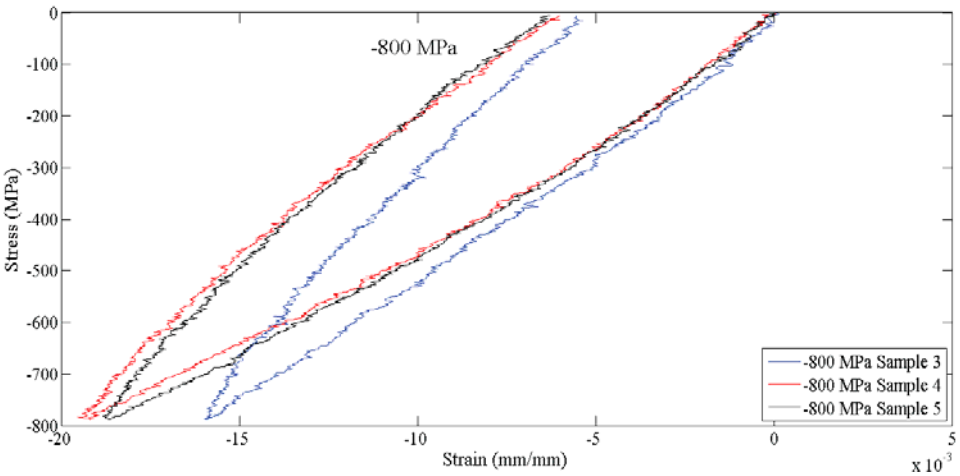

Figure 43.—Comparison of the responses of $Ni_{50.3}Ti_{33.7}Hf_{16}$ alloy Samples 3 to 5 subjected to Type B loading to –10306 N force (–800 MPa) for determination of the reproducibility of the test data and stability of the material (initial strains adjusted to zero).

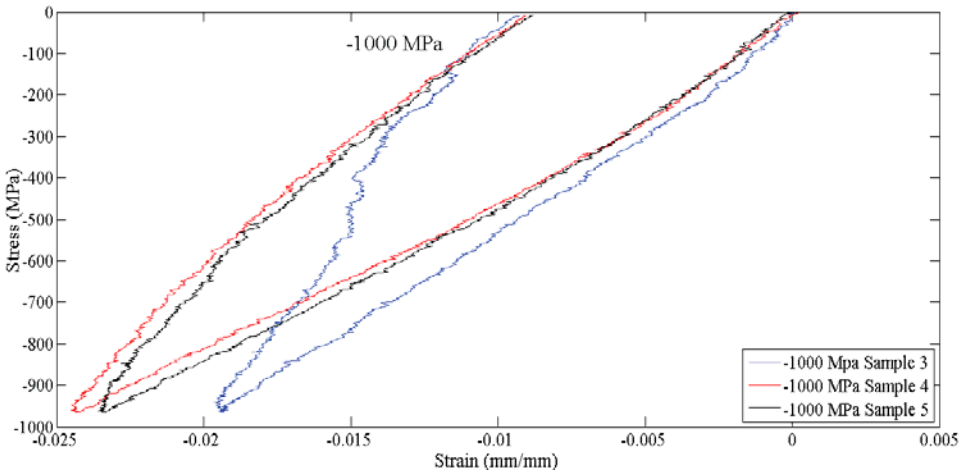

Figure 44.—Comparison of the responses of $Ni_{50.3}Ti_{33.7}Hf_{16}$ alloy Samples 3 to 5 subjected to Type B loading to –12882 N force (–1000 MPa) for determination of the reproducibility of the test data and stability of the material (initial strains adjusted to zero).

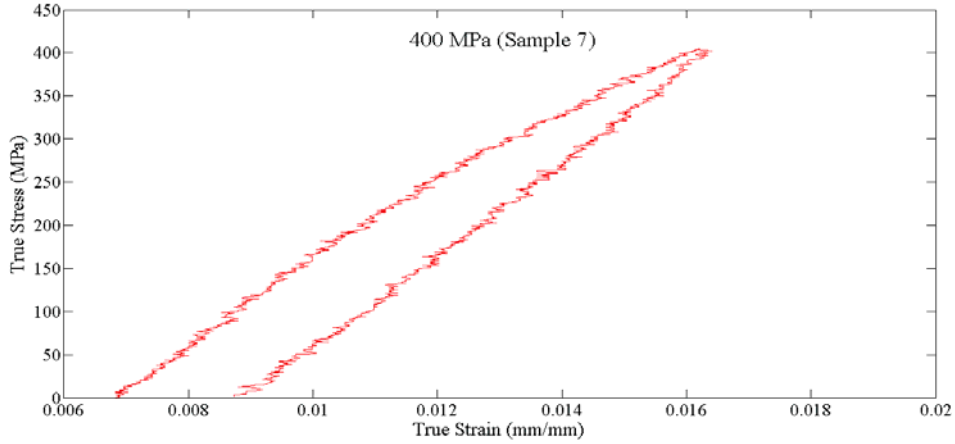

Figure 45.—Stress-strain responses of $Ni_{50.3}Ti_{33.7}Hf_{16}$ alloy Sample 7 subjected to Type B loading to 400 MPa.

Figure 45 is plot of a Type B loading test performed in tension at 400 MPa on Sample 7. The sample subsequently failed in the threads during the next cycle while loading to 600 MPa (Fig. 46). Consequently, the number of tension tests in the study was limited because of the tendency for the $Ni_{50.3}Ti_{33.7}Hf_{16}$ alloy to fail in the threads during tensile loading at stresses near 500 MPa.

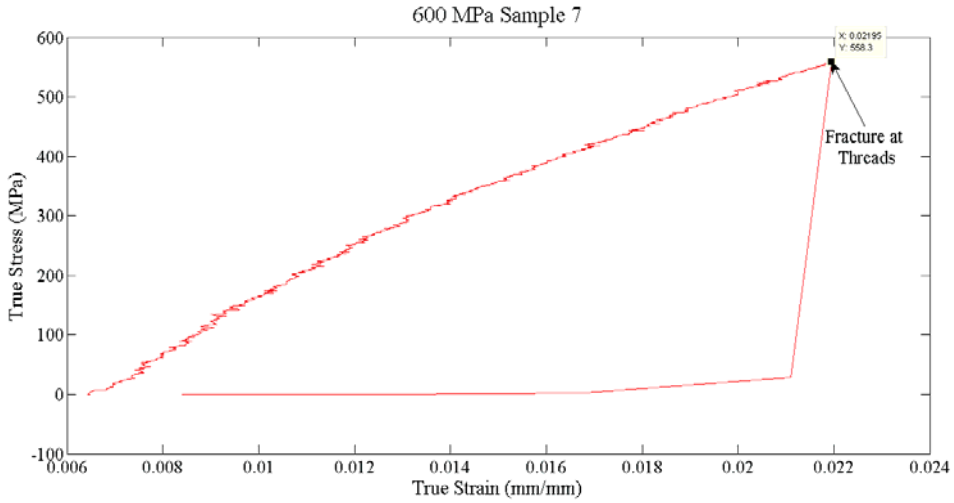

Figure 46.—Stress-strain response of $Ni_{50.3}Ti_{33.7}Hf_{16}$ alloy Sample 7 to failure while loaded in tension.

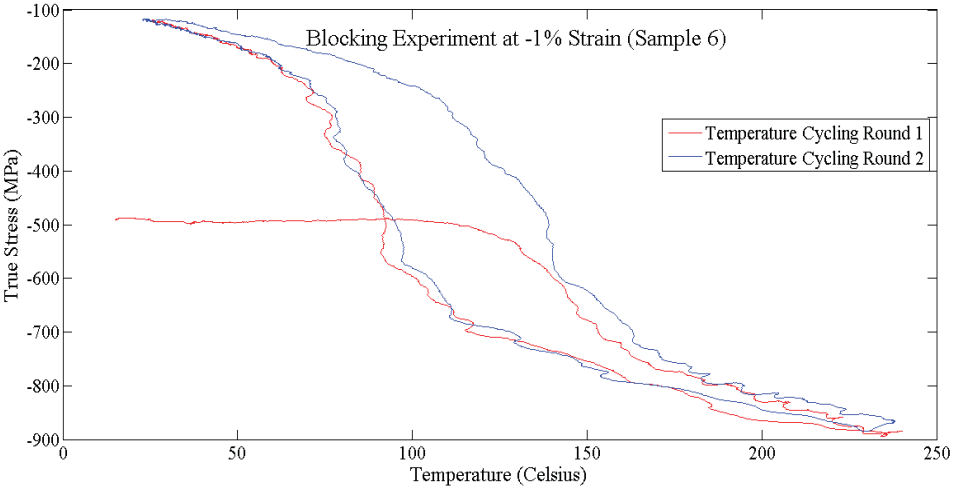

Figure 47.—Stress-temperature responses of $Ni_{50.3}Ti_{33.7}Hf_{16}$ alloy Sample 6 subjected to Type C loadings.

3.2.3 Type C Loading

Type C loading was performed on Samples 6 and 7. Figure 47 is the result obtained for a blocking experiment (Type C loading) performed on Sample 6 constrained at ~–1 percent strain during thermal cycling. Figure 48 is the result obtained for a similar blocking experiment performed on Sample 6 but constrained at ~–2.5 percent strain. During this experiment the axial force exceeded 13000 N (in compression) while temperature cycling, while the load frame's limit was 13000 N. Hence the load frame could not keep the crosshead fixed during the experiment and the blocking experiment could not be performed as required. The variation of strain with temperature is plotted in Figure 49 (which should have been a straight horizontal line if the limit of the test frame had not been exceeded) to show how much the test deviated from the desired limit. However, this result does indicate that very significant stresses are generated during the thermally induced martensite-to-austenite transformation in this material. Figure 50 is the result obtained for Type C loading (blocking experiment) performed on Sample 7 constrained at a much more modest ~–0.5 percent strain.

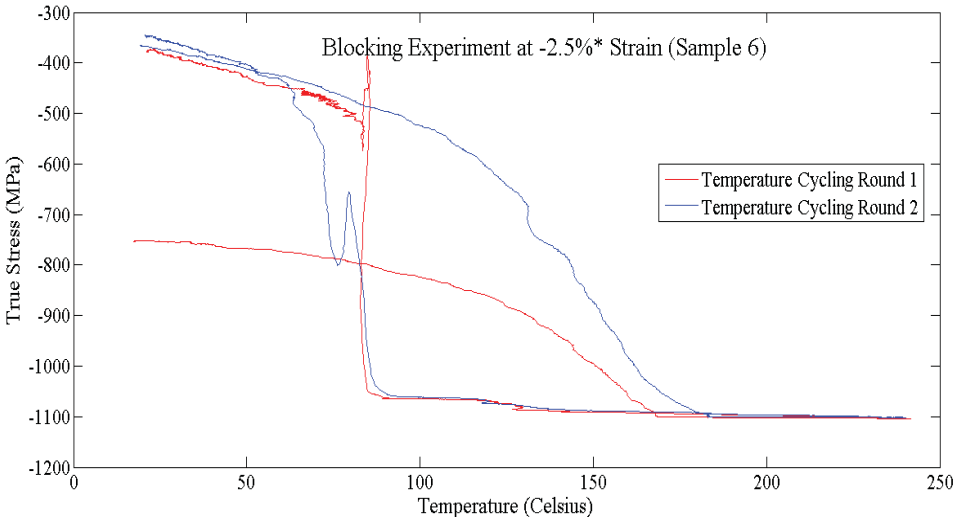

Figure 48.—Stress-temperature responses of $Ni_{50.3}Ti_{33.7}Hf_{16}$ alloy Sample 6 subjected to Type C loadings.

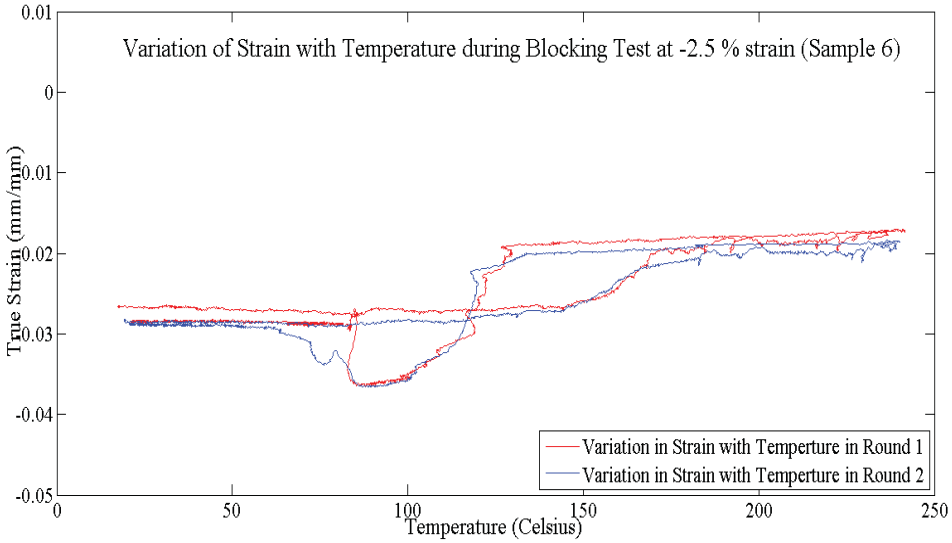

Figure 49.—Variation in strain while attempting to perform Type C loading on $Ni_{50.3}Ti_{33.7}Hf_{16}$ alloy Sample 6 as the load limit of the test frame was exceeded.

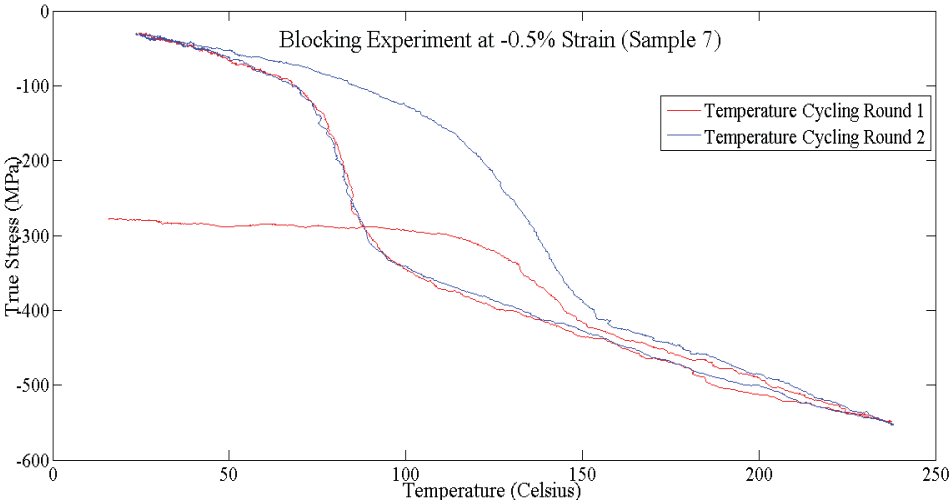

Figure 50.—Stress-temperature responses of $Ni_{50.3}Ti_{33.7}Hf_{16}$ alloy Sample 7 subjected to Type C loadings.

4.0 Discussion of Important Observations

Results from the Type I (proportional tension), shown in Figures 12 and 17, and Type II (proportional compression), shown in Figures 22 and 27, loading routines on the $Ni_{50.3}Ti_{29.7}Hf_{20}$ alloy, indicate that the transformation stress for the material is higher at 220 °C than at 180 °C. This suggests that for the $Ni_{50.3}Ti_{29.7}Hf_{20}$ alloy the stress-induced phase transformation from austenite to martensite occurs more easily at lower temperatures (within a temperature range above A_f) as stability of the austenite phase increases with temperature. This is consistent with the established understanding of the stress-temperature dependence of the martensitic transformation via the Clausius-Clapeyron relationship as applied to SMAs (Refs. 7 and 10). However, the fact that the stress-induced transformation for this alloy occurs at such high temperatures and in a stable manner, as previously confirmed in similar materials (Refs. 5, 7, and 8), is a significant advantage over binary NiTi alloys.

Figures 32 to 34 provide an indication of the phase transformation temperatures for the $Ni_{50.3}Ti_{33.7}Hf_{16}$ alloy as a function of applied stress. In particular, the phase transformation temperatures observed for the 16-at.% Hf alloy are ~60 °C less than those observed from Type A testing of previous $Ni_{50.3}Ti_{29.7}Hf_{20}$ alloys (Refs. 5, 7, and 9). Thus the effect of Hf concentration on phase transformation temperatures is apparent: an increase in Hf content leads to an increase in transformation temperatures. This is also consistent with the findings of Potapov et al. (Ref. 11).

What is much more interesting, is that the results indicate that increasing Hf content leads to an increase in tension and compression transformation strains, when comparing the results of the 16-at.% Hf alloy with the 20-at.% Hf results of Bigelow et al. (Ref. 5) and Benafan et al. (Ref. 9). For example, the 16-at.% Hf alloy exhibited ~1.5 percent tension, 1.25 percent compression transformation strains under 200 MPa load whereas the 20-at.% Hf alloy exhibited ~2.75 percent tension, 1.75 percent compression transformation strains under the same isobaric conditions (Ref. 5). The trend is also consistent for transformation strains under other loads. The 16-at.% Hf alloy, however, shows no signs of plastic deformation, or “open loop” strain under 1 GPa compressive loads (Fig. 33), while in unpublished research, Bigelow et al. have shown that the 20-at.% Hf alloy begins to exhibit open loop strain at loads of 800 MPa. This finding suggests that the 16-at.% Hf alloy is stronger.

In fact, we found that the macroscopic yield stress of the $Ni_{50.3}Ti_{33.7}Hf_{16}$ alloy is ~1600 MPa effective stress, independent of loading mode (Figs. 13, 23 to 26, and 28 to 31). This is significantly larger than the strength of binary NiTi, which ranges from 600 to 1200 MPa (Refs. 1 and 10). However, consistent with the Bigelow et al. result, we also observed the development of unrecovered strains due to plasticity-transformation interactions when the material was loaded in excess of 800 MPa but below the 1600 MPa

effective stress (Figs. 14 to 16 and 19 to 21) as the applied strain was not fully recovered during these loading sequences.

The other important observation is made from the plots in Figures 10, 11, and 13. The 'plateau' in the case of tension only, compression only, and torsion only loading of the $Ni_{50.3}Ti_{29.7}Hf_{20}$ alloy start at different equivalent stress values (noting that the equivalent stress—strain curve is essentially the same as an axial stress strain curve for Type I and II loading). Also, the transformation strains in all three types of loadings are different, the largest being the case of torsional loading. This suggests that the material is highly asymmetric. Also, the larger torsion transformation strain (7 percent shear strain width to the pseudoelastic plateau) than binary NiTi (~4 percent shear strain width to the pseudoelastic plateau (Ref. 12)) supports recent calculations of single crystal recoverable strains that show the 20-at.%Hf alloy to have ~175 percent of the potential for transformation strain relative to binary NiTi (Ref. 13). It is likely that further transformation strain may be achieved through polycrystalline texture optimization not only for torsion, but also tension and compression.

By studying axial and torsional stress—strain curves of Type IV and Type V loading tests on the $Ni_{50.3}Ti_{29.7}Hf_{20}$ alloy (Figs. 14 and 15), it can be observed that plastic strains obtained at the end of both tests in the axial and torsional curves differ even though the tests differ only in the sequence of unloading. The axial plastic strain is considerably higher in the case of Type IV loading (ATTA) compared to Type V loading (ATAT), while the torsional plastic strain is higher in the case of Type V loading compared to Type IV loading. This observation explains the need for studying the alloy's properties in different loading paths and supports the recent finding of Richards et al. that the development of plasticity is highly path-dependent when the plastic strain is less than or the same order of magnitude as the transformation strain (Ref. 14).

5.0 Conclusions

There are a number of primary conclusions concerning slightly Ni-rich, precipitation strengthened NiTiHf SMA that can be drawn from the results of this empirical study.

1. Increasing Hf content, even for slightly Ni-rich compositions, result in an increase in transformation temperatures (other factors being constant such as Ni content and aging condition).
2. Increasing Hf content actually results in increasing transformation strains.
3. The strength of the NiTiHf alloys is considerably higher than the strength of binary NiTi alloys.
4. The random textured NiTiHf alloy behaves differently in tension, compression, and torsion loading. For a random polycrystalline texture, the torsion performance is superior to binary NiTi, but tension and compression are inferior. However, new calculations (Ref. 12) have shown that through texture optimization, superior performance may be obtained in the other loading modes for NiTiHf alloys.
5. The development of plastic strain was path dependent for the cases studied in this investigation.

In addition, the pseudoelastic results obtained in this study for the 20-at.% Hf alloy complement the actuation characterization that has been previously performed (Refs. 5, 7, and 9). Combined, these data provide a complete actuation plus pseudoelasticity data set on a single high-temperature shape memory alloy, which should prove to be instrumental for calibrating SMA constitutive models in future work.

References

1. K. Otsuka and C.M. Wayman, Shape Memory Materials, Cambridge University Press, Cambridge, 1998.
2. K. Otsuka and X. Ren, Progress in Materials Science 50 (2005) 511–678.
3. K. Yamauchi, I. Ohkata, K. Tsuchiya, S. Miyazaki, Shape Memory and Superelastic Alloys: Technologies and Applications, Woodhead Publishing Limited, Cambridge, 2011.
4. P.E. Thoma, J.J. Boehm, Materials Science & Engineering A 273–275 (1999) 385–389.
5. G.S. Bigelow, A. Garg, S.A. Padula, D.J. Gaydosh, and R.D. Noebe, Scripta Materialia 64 (2011) 725–728.
6. A. Evirgen, F. Basner, I. Karamen, R. Noebe, J. Pons, and R. Santamarta, Functional Materials Letters 5 (2012) 1250038.
7. H.E. Karaca, S.M. Saghaian, G. Ded, H. Tobe, B. Basaran, H.J. Maier, R.D. Noebe, and Y.I. Chumlyakov, Acta Materialia 61 (2013) 7422–7431.
8. D.R. Coughlin, P.J. Phillips, G.S. Bigelow, A. Garg, R.D. Noebe and M.J. Mills, Scripta Materialia 67 (2012) 112–115.
9. O. Benafan, R.D. Noebe, S.A. Padula II, R. Vaidyanathan, Metallurgical & Materials Transactions 43 (2012) 4539–4552.
10. Q.P. Sun, K.C. Hwang, Journal of the Mechanics and Physics of Solids, 41 (1993) 1–17.
11. P.L. Potapov, A.V. Shelyakov, A.A. Gulyaev, E.L. Svistunova, N.M Matveeva, D. Hodgson, Materials Letters 32 (1997) 247–250.
12. P. Thamburaja, L. Anand International Journal of Plasticity 18 (2002) 1607–1617.
13. J. Yang and A.P. Stebner, (2013) Unpublished Research.
14. A.W. Richards, R.A. Lebensohn, K. Bhattacharya, Acta Materialia 61 (2013) 4384–4397.